Open Research Online

The Open University's repository of research publications
and other research outputs

Variations in color and reflectance on the surface of asteroid (101955) Bennu

Journal Item

How to cite:

DellaGiustina, D. N.; Burke, K. N.; Walsh, K. J.; Smith, P. H.; Golish, D. R.; Bierhaus, E. B.; Ballouz, R.-L.; Becker, T. L.; Campins, H.; Tatsumi, E.; Yumoto, K.; Sugita, S.; Deshapriya, J. D. Prasanna; Cloutis, E. A.; Clark, B. E.; Hendrix, A. R.; Sen, A.; Al Asad, M. M.; Daly, M. G.; Applin, D. M.; Avdellidou, C.; Barucci, M. A.; Becker, K. J.; Bennett, C. A.; Bottke, W. F.; Brodbeck, J. I.; Connolly, H. C.; Delbo, M.; de Leon, J.; Drouet d'Aubigny, C. Y.; Edmundson, K. L.; Fornasier, S.; Hamilton, V. E.; Hasselmann, P. H.; Hergenrother, C. W.; Howell, E. S.; Jawin, E. R.; Kaplan, H. H.; Le Corre, L.; Lim, L. F.; Li, J. Y.; Michel, P.; Molaro, J. L.; Nolan, M. C.; Nolau, J.; Pajola, M.; Parkinson, A.; Popescu, M.; Porter, N. A.; Rizk, B.; Rizos, J. L.; Ryan, A. J.; Rozitis, B.; Shultz, N. K.; Simon, A. A.; Trang, D.; Van Auken, R. B.; Wolner, C. W. V. and Lauretta, D. S. (2020). Variations in color and reflectance on the surface of asteroid (101955) Bennu. Science, 370(6517)

For guidance on citations see FAQs.

© 2020 The Authors

https://creativecommons.org/licenses/by-nc-nd/4.0/

Version: Accepted Manuscript

Link(s) to article on publisher's website:
http://dx.doi.org/doi:10.1126/science.abc3660

Copyright and Moral Rights for the articles on this site are retained by the individual authors and/or other copyright owners. For more information on Open Research Online's data policy on reuse of materials please consult the policies page.

oro.open.ac.uk

Variations in Color and Reflectance on the Surface of Asteroid (101955) Bennu

D.N. DellaGiustina[1,2*], K.N. Burke[1], K.J. Walsh[3], P.H. Smith[1], D.R. Golish[1], E.B. Bierhaus[4], R.-L. Ballouz[1], T. L. Becker[1], H. Campins[5], E. Tatsumi[6,7], K. Yumoto[7], S. Sugita[7], J.D. Prasanna Deshapriya[8], E.A. Cloutis[9], B.E. Clark[10], A.R. Hendrix[11], A. Sen[10], M. M. Al Asad[12], M.G. Daly[13], D.M. Applin[9], C. Avdellidou[14], M.A. Barucci[8], K. J. Becker[1], C.A. Bennett[1], W.F. Bottke[3], J.I. Brodbeck[1], H.C. Connolly Jr.[15], M. Delbo[14], J. de Leon[6], C.Y. Drouet d'Aubigny[1], K.L. Edmundson[1], S. Fornasier[8,16], V.E. Hamilton[3], P.H. Hasselmann[8], C.W. Hergenrother[1], E.S. Howell[1], E.R. Jawin[17], H.H. Kaplan[18], L. Le Corre[11], L. F. Lim[17], J.Y. Li[11], P. Michel[14], J.L. Molaro[11], M.C. Nolan[1], J. Nolau[4], M. Pajola[19], A. Parkinson[9], M. Popescu[20,6], N.A. Porter[1], B. Rizk[1], J.L. Rizos[6], A. J. Ryan[1], B. Rozitis[21], N. K. Shultz[1], A.A. Simon[18], D. Trang[22], R.B. Van Auken[1], C.W.V. Wolner [1], and D.S. Lauretta[1]

Affiliations:

[1]Lunar and Planetary Laboratory, University of Arizona, Tucson, AZ, USA

[2]Department of Geosciences, University of Arizona, Tucson, AZ, USA.

[3]Southwest Research Institute, Boulder, CO, USA.

[4]Lockheed Martin Space, Littleton, CO, United States

[5]Department of Physics, University of Central Florida, Orlando, FL, USA.

[6]Instituto de Astrofísica de Canarias and Departamento de Astrofísica, Universidad de La Laguna, Tenerife, Spain.

[7]University of Tokyo, Tokyo, 113-0033, Japan

[8] LESIA (Laboratoire d'Etudes Spatiales et d'Instrumentation en Astrophysique), Observatoire de Paris, Université PSL (Paris Sciences & Lettres), CNRS (Centre national de la recherche scientifique), Université de Paris, Sorbonne Université, 92195 Meudon, France.

[9] Department of Geography, University of Winnipeg, Winnipeg, MB R3B 2E9, Canada

[10]Department of Physics and Astronomy, Ithaca College, Ithaca, NY, USA.

[11]Planetary Science Institute, Tucson, AZ, USA.

[12]Department of Earth, Ocean and Atmospheric Sciences, University of British Columbia, Vancouver, BC, Canada.

[13]The Centre for Research in Earth and Space Science, York University, Toronto, ON, Canada

[14] Université Côte d'Azur, Observatoire de la Côte d'Azur, CNRS, Laboratoire Lagrange, Nice, France.

[15] Department of Geology, Rowan University, Glassboro, NJ, USA.

[16] Institut Universitaire de France (IUF), 1 rue Descartes, 75231 Paris CEDEX 05, France.

[17] Smithsonian Institution National Museum of Natural History, Washington, DC, USA.

[18] NASA Goddard Space Flight Center, Greenbelt, MD, USA.

[19] Istituto Nazionale di Astrofisica (INAF), Osservatorio Astronomico di Padova, Padua, Italy

[20]Astronomical Institute of the Romanian Academy, Bucharest, Romania.

[21]The School of Physical Sciences, The Open University, Milton Keynes, UK.

[22]University of Hawai‘i at Mānoa, Hawai‘i Institute of Geophysics and Planetology, Honolulu, HI, USA.

*Correspondence to: danidg@lpl.arizona.edu

Abstract: Visible-wavelength color and reflectance provide information about the geologic history of planetary surfaces. We present multispectral images (0.44 to 0.89 microns) of near-Earth asteroid (101955) Bennu. The surface has variable colors overlain on a moderately blue global terrain. Two primary boulder types are distinguishable by their reflectance and texture. Space weathering of Bennu surface materials does not simply progress from red to blue (or vice versa). Instead, freshly exposed, redder surfaces initially brighten in the near-ultraviolet (become bluer at shorter wavelengths), then brighten in the visible to near-infrared, leading to Bennu's moderately blue average color. Craters indicate that the timescale of these color changes is ~10^5 years. We attribute the reflectance and color variation to a combination of primordial heterogeneity and varying exposure ages.

Main Text

The near-Earth asteroid (101955) Bennu is the target of the Origins, Spectral Interpretation, Resource Identification, and Security–Regolith Explorer (OSIRIS-REx) sample-return spacecraft (*1*). Prior to launch, telescopic observations of Bennu had identified it as a low-albedo object—potentially indicating a carbon-rich composition—with a featureless, gently blue spectrum (blue signifies a negative spectral slope with respect to the solar spectrum, whereas red signifies a positive slope). This resulted in its classification as a blue (B-type) asteroid *(2)*, a subclass of the broader carbonaceous (C-complex) group of small bodies. Bennu is a rubble-pile asteroid (*3–6*), accumulated from fragments of a larger parent body that was shattered by a catastrophic impact in the inner main asteroid belt ~1 Ga ago (*3*). Bennu eventually migrated from the main belt into its current orbit in near-Earth space (*3*).

OSIRIS-REx measurements acquired during the initial phases of the mission showed that Bennu is dominated by hydrated clay-bearing minerals (phyllosilicates) and magnetite (*7*), indicating that water was present on and altered the composition of Bennu's parent body (aqueous alteration). Organic compounds and carbonates have been discovered across the asteroid's surface, supporting the hypothesis that B-type asteroids are carbon-rich (*8, 9*). Carbon-bearing species are optically opaque (as is magnetite) so could be responsible for Bennu's low global normal albedo of 0.044 (*4,10*). These findings suggest that Bennu's composition may be representative of the primitive bodies that delivered water and organic molecules to the early Earth (*11*).

Although the initial composition of an asteroid influences its global colors, physical properties such as particle size, surface roughness, and porosity can also influence these spectral characteristics, as can duration of exposure to the space environment. The surface colors of airless bodies are expected to be heavily altered by space weathering processes (*12, 13*), including bombardment by solar wind particles and meteoroids. On anhydrous planetary surfaces, such as the Moon and stony (S-type) asteroids, space weathering darkens and reddens spectral slopes in the visible and near-infrared (e.g., *12, 14*). However, on primitive carbonaceous asteroids such as Bennu, and their meteorite analogs, space weathering effects are not well understood. Measured colors of primitive asteroids do not show consistent spectral relationships with surface exposure age (*13, 15, 16, 17*), nor do laboratory experiments of simulated space weathering on analogous meteorite and phyllosilicate samples: Some studies indicate that space weathering leads to bluing (*13, 18-22*), but others find that it leads to reddening (*16*, *20, 23, 24*). This is likely because the initial composition and the physical structure of the materials play a role in the spectral changes observed (*16*, *20*). To determine how space weathering affects low-albedo carbonaceous asteroids, we searched for a correlation between Bennu's colors and the age of its surface features determined from morphology. The spatial distribution and geologic setting of varying colors on Bennu may also aid our understanding of the composition and evolution of the asteroid's surface.

Color observations of Bennu

OSIRIS-REx obtained color observations of Bennu during two hyperbolic flybys on 14 March and 26 September 2019, as part of the Baseball Diamond phase of the mission's Detailed Survey (*23*). The OSIRIS-REx Camera Suite (OCAMS) (*26*) was used to acquire color images using the multispectral MapCam imager, which has four bands in the visible (VIS; 0.40–0.70 μm) and near-

infrared (NIR; 0.70–2.5 μm) wavelengths. The MapCam bands—*b′* (0.44–0.50 μm), *v* (0.52–0.58 μm), *w* (0.67–0.73 μm), and *x* (0.82–0.89 μm)—are similar to those used by telescopic asteroid surveys (*27*) to infer asteroid composition and classify their spectra (*28*). Most asteroid observations have been limited to unresolved disk-integrated (globally averaged) spectra. We use spatially resolved MapCam color images (pixel scale ~25 cm) to investigate reflectance and color across Bennu's surface. To establish relationships between color and surface morphology, we pair these color observations with higher resolution OCAMS PolyCam panchromatic images (2 to 5 cm pixel^{-1}) of the same locations.

We radiometrically calibrated the MapCam and PolyCam images to units of reflectance (also known as radiance factor or *I/F*) (*29*). MapCam images were corrected to normal viewing conditions (0° solar incidence, 0° solar phase, and 0° observer emission angles) using a Robotic Lunar Observatory photometric function to assess albedo differences across the surface (*30, 31*). We subsequently map-projected and mosaicked the MapCam images using cartographic techniques developed for irregular planetary bodies (*23,31,32*). Band ratios and principal component analysis (PCA) were used to identify variations in multispectral images and distinguish regions with distinct spectral properties (*29*). To establish statistically meaningful relationships between color, reflectance, and morphological features, we mapped ~1600 boulders and ~700 craters, then extracted their median spectra using established methods (*31, 4, 33*). We assessed spectral variations that were bounded by irregular morphological features using centimeter-scale 3D digital terrain models produced with data from the OSIRIS-REx Laser Altimeter (OLA) (*34-36*). We also compared our findings with near-infrared hyperspectral data acquired at lower spatial resolution using the OSIRIS-REx Visible and InfraRed Spectrometer (OVIRS) (*37*).

Bennu's global photometric spectrum is moderately blue (spectral slope of –0.1701 μm^{-1}) in MapCam data (0.44 to 0.89 μm), but spectral slopes vary from blue (negative, –0.25 μm^{-1}) to red (positive, 0.05 μm^{-1}) at spatial scales of as small as 2 m (Fig. 1). Bennu's surface exhibits widespread heterogeneity in reflectance (Figs. 1 and 2). PCA shows that the first principal component (PC1) corresponds to albedo, whereas the second principal component (PC2) corresponds to changes in the overall spectral slope (from *b′* to *x*), and PC3 indicates variation in the near-ultraviolet (from *b′* to *v*) (figs. S1 to S3).

Bennu's globally blue surface is dominated by a coarse layer of decimeter- to meter-scale rocks with some centimeter-scale particles (regolith), which we refer to as average terrain. The spectral variability is associated with distinct geologic features, including boulders, craters, and areas of mass wasting (rock movement down geopotential slopes), which we use to distinguish color units on the asteroid (Table 1 and fig. S4, A and B). These units provide a framework for classifying commonly observed features on the surface.

Boulders on Bennu

Boulders are the primary source of heterogeneity on Bennu. Some individual boulders have VIS-NIR absorption features at 0.55 μm (as previously observed (*5*)), 0.7 μm (Fig. 2D), and near 1 μm (as previously observed (*38*)). There are also outliers among the boulder population that do not correspond with a specific color unit.

Boulders have a wide range of normal reflectance values (0.032 to at least 0.26 (*38*)) that are multi-modally distributed with two prominent peaks (Fig. 2A). The reflectance of boulders is not normally distributed and is most consistent with four Gaussians (*31*), or perhaps two or more non-Gaussian components. We refer to boulders as bright or dark based on whether they are brighter or darker than the median reflectance of 0.049, which lies between the two prominent peaks of the reflectance distribution.

Bright boulders have smooth surfaces, typically angular shapes, and have blue spectral slopes in the mid-VIS to NIR (MapCam *v* to *x* bands). However, unlike the average terrain, ~80% of the bright boulders are dark in the near-ultraviolet (near-UV; $b'/v < 1$; Fig. 2, fig. S4 A and B). The bright boulders (Fig. 3, A and B) appear to have similar sizes (are well-sorted) with diameters <10 m.

Dark boulders (reflectance ≤0.049) span a range of visible spectral slopes but are generally redder than the bright boulders in the mid-VIS to NIR wavelengths (Figs. 1 and 2, A and B). The dark boulders are less angular than bright boulders and commonly have rougher, more undulating surface textures (Fig. 3, C and D). They encompass a wide range of sizes (from decimeters to ~95 m) and include all the large (≳20 m) boulders on the asteroid. Although the average terrain lies between the bright and dark populations, dark boulders and smaller dark particles (presumably formed by boulder breakdown) appear to be the dominant material; this is illustrated by the close correspondence between Bennu's average reflectance (0.0439 ± 0.002) and the reflectance peak of the dark boulder population (0.0450 ± 0.002) (Fig. 2A, gray dashed line).

Color variation is also evident within individual boulders (Figs. 1 and 3). Sometimes this occurs between faces of an individual rock, usually large dark boulders (Fig. 3, C to H). These examples of intra-boulder color variation are associated with apparent exfoliation and fracturing of the rock (*39*) (Fig. 3, G and H) and in textures akin to weathering rinds—exterior crusts that appear discolored compared to faces that are potentially more recently exposed (Fig. 3, C and G). We also observe boulders that appear to be breccias, that is, composed of rock fragments cemented together as a result of large impacts on Bennu's parent body (*33, 38)*. In these boulders, spectrophotometrically distinguishable fragments (clasts) are embedded in a host matrix that has similar texture, reflectance, and color to the dark boulders (Fig. 3, E and F).

A small population of boulders with very high reflectance (up to 0.26 (*38*)) shows evidence of an absorption feature at 1 μm (downturn in the *x* band). OVIRS data indicates that these boulders contain pyroxene (*38*). Pyroxene-bearing material appears in distinct clasts embedded within larger host rocks whose color and reflectance are similar to those of the dark boulders (Fig. 3I (*38*)); it also appears in smaller (meter-scale), isolated boulders that do not look brecciated. Pyroxene was probably inherited from Bennu's parent body, where it was implanted by an impactor that may have originated from a fragment of (4) Vesta (*38*), the differentiated (not primitive) inner main-belt asteroid visited by the Dawn mission (*40*). Although their reflectance overlaps with that of the bright boulders, and their texture is like that of the breccias, we separate pyroxene-bearing boulders into their own category (Table 1) based on their distinct spectral shape in the VIS to NIR (*v* to *x*; Fig. 2, B and C).

Some boulders have an absorption feature at 0.7 μm (absorption depth of 2 to 10%). Similar absorption features have been observed in spectra of primitive asteroids and carbonaceous meteorites, where it was attributed to iron in some clay-bearing phyllosilicates (*41*). Boulders with the deepest absorptions at this wavelength span a wide range of reflectance (0.0364 to 0.0811); however, most (~60%) dark boulders tend to have a shallow (~1%) 0.7-μm absorption. Although this is at the limit of the 1% relative precision of OCAMS data (*29*), it is spatially coherent with individual boulders, giving us confidence that the feature is real (fig. S5).

Color and surface processes

Some areas of the surface are brighter in the near-UV (i.e., an upturn in the near-UV *b′* band; $b'/v > 1.01$, or 1% greater than average), which we refer to as blue units. One of the bluest contiguous surfaces on Bennu is the eastern side of the boulder shown in Fig. 3G. Digital terrain models show this rock face is recessed relative to the western face of the boulder (Fig. 3H), and color data indicate that the recessed face has a steeper blue spectral slope. Conversely, the western face of the boulder is brighter and has a more neutral spectral slope, similar to the global average (fig. S4C). The bluer, recessed eastern face may be a fresher surface, more recently exposed to the space environment by thermal fracturing or exfoliation—ongoing surface processes on Bennu (*39, 42*). Similar patterns are observed on other boulders that appear to have been recently exfoliated (as indicated by layers with different relief). We also observe bluer-than-average near-UV slopes on the high-elevation rims (10 to 20 m higher than surrounding terrains) of equatorial craters that show recent indications of mass wasting (Fig. 4, A and B) (*43*).

The correspondence between blue units and potentially less weathered surfaces suggests that enhanced near-UV reflectance is related to younger exposure ages on Bennu. The blue units are correlated with the relative band depth at 0.55 μm (fig. S6), indicating that the upturn observed in the near-UV index may be the result of an absorption feature at 0.55 μm. This absorption feature on Bennu has previously been attributed to magnetite (*5*), which is also detected in thermal emissivity spectra from OTES (*7*). However, this absorption feature could also result from graphitized carbon (*44*), and both magnetite and graphite are associated with space weathering (discussed further below).

The color of the largest craters (>100 m) on Bennu is indistinguishable from that of the average terrain. However, many small (≤25 m) craters are redder than the Bennu's average by ≥0.5σ in the near-UV to NIR, where σ is the full-width at half maximum of the global distribution of *b′* to *x* spectral slopes (Fig. 4, C and D; Fig. 5, A and B). We refer to these as small reddish craters. By contrast, we identified no craters bluer than ≤ 0.5σ from Bennu's global average *b′* to *x* spectral slope (Fig. 5A).

The size-frequency distribution of reddish craters implies that they are one of the youngest components of the global crater population (Fig. 5C). If so, we expect that reddish craters are among to the youngest surface features on Bennu (unlike the blue units described above). The absolute spectral slopes of the reddish craters appear to correspond with crater size (Fig. 5, A and B), and these craters are also darker than the global average (Fig. 5, D). In PolyCam images, the reddish craters display a texture distinct from the bulk of Bennu's surface: unresolved at the pixel scale (i.e., <5 cm), indicating fine-particulate material (fig. S7). The largest examples of reddish

craters exist at mid to high latitudes (poleward of ± 20°), including the crater selected as the primary OSIRIS-REx sample collection site, Nightingale (56°N, 42°E).

Evidence of freshly exposed material on Bennu

Reddish craters and blue units on Bennu both correspond to apparently young exposure ages (Figs. 3, G and H, and 4, C and D). To resolve this apparent contradiction, we consider crater production rates and size-scaling laws, stratigraphic relationships, and potential contributors to spectral slopes other than exposure age.

The size-frequency distribution of the reddish craters has a power-law index of –2.1 ± 0.4 (*31*). The power-law index of the reddest subset of these craters (b' to x spectral slopes ≥1σ from the global median value of –0.0698 μm^{-1}) is –2.3 ± 0.6 (*31*). These values are close to that of the expected production of craters in the present-day main asteroid belt and near-Earth space over the last 100,000 years (predicted power-law index between –2.6 and –2.7; Fig. 5C) (*47-48*). The global crater population has a different power-law index of –1.1 ± 0.1 (*31*). At small diameters, the distributions of the reddish craters do not deviate from that of the expected crater production (Fig. 5C), unlike the global population of craters on Bennu (*33*) and nearly all other closely studied small bodies (*49*). A mismatch at small diameters between observed crater populations and the expected crater production has been attributed to erasure processes (*49)*, which efficiently erode and diminish small craters. The correspondence between the expected production of the red craters on Bennu and their actual distribution supports a young age: Unlike the global crater distribution, they have not yet experienced substantial erasure.

We estimate the time required to produce the craters on Bennu using a crater production rate and a scaling law for crater size from impactor size (*31*). Assuming that the red craters have formed since Bennu's arrival in the inner Solar System, we adopt the established crater production rate from the near-Earth object population (*47, 48*). Crater scaling relationships, however, are less certain owing to unknown material properties and the structure of rubble-pile asteroids. The Small Carry-on Impactor (SCI) experiment performed on asteroid Ryugu by the Hayabusa2 mission (*50*) showed that small impactors (~30 cm) can produce craters consistent with scaling laws that depend on gravity; craters formed in this gravity regime can be many times larger than the sizes expected from scaling laws governed by target material strength. The sizes of the reddish craters on Bennu are less than or similar to the diameter of the SCI crater (~18 m) (*50*). If gravity dominates the cratering process for small craters on Bennu (e.g., *51*), the reddest subset of these craters are less than 10^5 years old (Fig. 5C). This is consistent with the expected timescales of space weathering on near-Earth asteroids (~10^5 years) based on returned samples of asteroid Itokawa (*52*) and laboratory experiments on primitive meteorites (*20*). Thus, it is plausible that the reddish craters are the most recent areas of surface exposure and represent the least weathered material on Bennu.

Although recent surface exposure may explain the reddish craters on Bennu, in carbonaceous meteorites, redder spectral slopes in the VIS-NIR can also arise from fine particle sizes (<100 μm) (*53*). The smooth and unresolved appearance of the reddish craters on Bennu suggests that they possess finer-scale regolith (fines) than elsewhere on the surface (fig. S7). However, small craters on boulders also appear redder than the global average photometric spectrum, indicating that particle size is not the only factor (fig. S8). When the electrostatic forces acting on particles exceed

that of gravity and cohesion—as is often the case for micron-sized grains on asteroids—lofting occurs and preferentially removes fines (*54*). Simulations of electrostatic lofting show that detachment and escape of sub-millimeter particles is feasible on Bennu and likely occurs shortly after the formation of such fines (*54*). Although particle sizes <100 μm could contribute to reddening on Bennu, we anticipate that the loss of fines takes place on shorter timescales than the age of the reddish craters. However, if micron-scale particles are closely associated with freshly exposed materials, they could also produce the observed reddening.

Longer infrared wavelengths also indicate younger exposure ages for reddish craters. The shape of the 2.7 μm hydration feature, which is ubiquitous on Bennu (*7*), is sharper and shifts to shorter wavelengths within reddish craters, including the Nightingale sample site (fig. S9A). This is consistent with laboratory space weathering experiments performed on carbonaceous meteorites (*20*), which show that the minimum of the hydration feature at ~2.7 μm moves toward longer wavelengths with prolonged exposure to space weathering processes. Thus, sharper band features with shorter minimum wavelengths within craters may signify more recent exposure. The blue equatorial crater at 1.06°N, 152.75°E (Fig. 4, A and B) appears to have a sharper absorption feature but a band minimum similar to the global average (fig. S9B), indicating that it may have an intermediate exposure age. Unlike spectral slope, the shape of this spectral signature is not expected to be influenced by particle size (*20*).

The exposure age is less clear for the bluer-than-average, apparently broken boulder face in Fig. 3, G and H. We can set some constraints from the blue units associated with equatorial craters. Since its time in near-Earth space, Bennu's rotation rate has accelerated in response to surface scattering of sunlight and the emission of its own thermal radiation (*10, 55*), consequences of the Yarkovsky–O'Keefe–Radzievskii–Paddack (YORP) effect. The locations of two of the bluest craters (1.06°S, 152.75°E and 3.05°S, 128.79°E) correspond to an isolated equatorial region that experienced increased surface accelerations as Bennu's spin period decreased from 5 hours to the present-day 4.3 hours (fig. S10) (*10, 55*), suggesting that this area has experienced surface mass movement at some point in the past 200,000 years (*43*). Thus, we infer that that the exposure age of blue units is ~200,000 years.

Bue unit craters have also been overprinted by small reddish craters (Fig. 4D); we therefore presume that they are composed of the same underlying material, and that the blue unit craters are older than the reddish craters. This color trend of bluing with exposure time is consistent with some spectral studies of space weathering of carbonaceous meteorites (e.g.*,18-22*), but not previous surface-resolved observations of asteroids.

We suggest that nonlinear space weathering occurs on Bennu's surface. In this scenario, freshly exposed material is initially redder than the bulk of Bennu in the near-UV to NIR wavelengths (*b′* to *x*) (first stage). During early space weathering, these surfaces brighten more rapidly in the near-UV (*b′*) than in the mid-VIS to NIR (*v* to *x*), thereby increasing the *b′/v* band ratio (middle stage). This near-UV bluing may result from the deepening of an absorption near 0.55 μm, implying that magnetite or graphite abundance increases during the early stages of space weathering. Eventually, however, these color differences neutralize as the surface is brightened across the wavelengths observed by MapCam, and the downturn at 0.55 μm (*v* band) diminishes, leading to the gently blue

spectral slope that characterizes Bennu's global photometric spectrum and the oldest craters (final stage).

This space weathering progression is illustrated by craters that have been categorized on the basis of their spectral slope (Fig. 6). The first and middle stages are illustrated by the small reddish craters overprinted on blue equatorial craters (Fig. 4D). The middle and final stages may also be illustrated by the boulder in Fig. 3G, whose higher-relief, presumably older western face is brighter and has a more neutral spectral slope than the more recently exposed, bluer face. The final stage is illustrated by Bennu's average terrain.

The orientation of intra-boulder color variation provides further evidence of space weathering on Bennu. We examined 220 boulders with sizes $\gtrapprox$ 5 m in the equatorial region (20°S to 20°N), where MapCam images have the most consistent viewing conditions, and calculated the azimuthal angle that maximizes blue-to-red color variation across each boulder (*31*). Fig. S11 shows the latitude of boulders with large color variation (b' to x slope difference of >0.05 μm^{-1} between the two regions) as a function of the azimuthal angle of the blue-to-red direction (*31*). Bluer faces are preferentially oriented toward the equator (fig. S12). This may relate to solar exposure (e.g., heating or irradiation) and/or meteoroid bombardment, all processes that would preferentially affect equatorial latitudes (*42, 56*). We only observe this intra-color variation on dark boulders, perhaps owing to their larger sizes compared to other boulder types, or a different initial composition.

Mechanisms for space weathering on Bennu

Dark, optically opaque minerals (hereafter, opaques), such as nanophase iron, graphitized carbon, sulfides, and magnetite, are commonly produced by space weathering of primitive materials (*19, 19, 23, 44, 57*). Laboratory studies have shown that phyllosilicates intimately mixed with certain carbon species (including graphite) and magnetite can lead to bluer and darker spectral slopes in the visible wavelengths (*44*) (fig. S4C and D). The link between bluing opaque minerals and space weathering implies that blue spectral slopes are the result of a mature, weathered regolith on primitive B-type asteroids, although they cannot fully explain the brightening in the near-UV to NIR observed on Bennu.

As discussed above, studies of primitive asteroids and meteorites have contradictorily predicted both bluing and reddening with increased space weathering (e.g., *13-24*). Ion and meteoroid bombardment lead to darkening and reddening of anhydrous silicate planetary surfaces; this has previously been attributed to the accumulation of nanophase and larger metallic iron particles, which form in response to the space environment (*58*). However, contrary to the bluing and darkening predicted from the production of graphitized carbon and magnetite, the formation of nanophase iron in low-albedo asteroids such as Bennu may have a reddening and brightening effect, owing to the higher reflectance of nanophase iron than that of the primitive materials found in carbonaceous meteorites (*59*).

Space weathering trends observed on Bennu corroborate earlier studies (*13, 44*) that found that primitive asteroids, though dark relative to the asteroid population, are brighter in the UV than their primitive meteorite counterparts—that is, they are spectrally bluer at shorter wavelengths. Ion bombardment of primitive low-albedo meteorites in the laboratory leads to spectral bluing and

brightening (*20*). These spectral changes are attributed to the process of carbonization, whereby hydrogen is lost and crystalline carbon structures, such as graphite, are formed (*57)*. Irradiation experiments on complex hydrocarbons have shown that carbonization can induce metal-like optical properties in carbonaceous material, which leads to bluing and brightening (*17, 57*). We propose that space weathering–induced carbonization or magnetite formation may have influenced the surface colors on Bennu, especially in dark materials that become bluer (from the *v* to *x* bands) and brighter (across all bands) with increased exposure age.

Evidence for parent body heterogeneity

Although space weathering may influence the spectral slopes on Bennu, the disparate boulder populations that we identify—which differ in terms of their reflectance, texture, and size—suggest that some of Bennu's heterogeneity was inherited from its parent body. Dark boulders show a monotonic relationship of decreasing reflectance with increasing (redder) spectral slope, which is distinguishable from that of their bright counterparts (Fig. 2B) (*31*). Because space weathering is likely controlled by initial texture and composition, the difference in spectral slope trends between dark and bright boulders could result from the maturation of geologically distinct materials. Likewise, the less varied spectrophotometric properties of the bright boulders suggest that they are less susceptible to modification from space weathering or change on a different timescale (Fig. 2).

Heterogeneity in boulder reflectance on Bennu may be the result of distinct rock types that fragment differently, leading to an observed difference in their size-frequency distributions *(4*). Different compositions of the dark versus bright boulders may account for the correlation between reflectance and thermal properties for boulders on Bennu (*60*). The dark boulders have lower thermal inertia, which is attributed to higher porosity (*60*), consistent with their rougher and more crumbly (friable) appearance (Fig. 3, C and D). Conversely, the apparently smoother, more consolidated and angular bright boulders (Fig. 3, A and B) tend to have higher thermal inertias, attributed to lower porosity (*60*). Distinct texture and porosity can follow from differing mineralogy, levels of compaction, or heating and aqueous alteration histories.

The average blue spectrum of Bennu is consistent with serpentine or magnetite and serpentine, with some carbon (fig. S4, C and D). This composition is similar to that of Bennu's presumed meteorite analogs, the CM and CI groups of carbonaceous chondrites, which are dominated by Fe- and Mg-bearing phyllosilicates, respectively. In the most intensely aqueously altered CI chondrites, the Fe is contained in oxides, sulfides, carbonates, and other minor species (*61, 62, 63*).

The tendency of dark boulders to be slightly redder and brighter in the near-UV (Fig. 2, A to C) may indicate that they have a higher overall abundance of organic molecules, compared to their bright counterparts. This composition manifests as lower reflectance and redder slopes in more freshly exposed surfaces, which develop into steeper blue slopes during the early stages of space weathering. This, along with the weak 0.7-μm absorption sometimes present in dark boulders (Fig. 2D), is indicative of a higher proportion of Fe-bearing phyllosilicates than other boulders and implies that they represent a population of material from Bennu's parent body that has experienced less aqueous alteration. A correlation between lower reflectance and a 0.7-μm absorption band is

consistent with moderately altered CM carbonaceous chondrites, which are among the darkest primitive meteorites with a nearly ubiquitous a 0.7-μm absorption feature (*64*).

Some bright boulders contain veins of brighter material, which may be composed of carbonates (*9*). This implies a level of aqueous alteration that should also lead to the formation of magnetite (*65*). The lack of a near-UV upturn in carbonate-bearing boulders could signify that other phases influence their spectral characteristics. For example, bright boulders may be dominated by a hydrated mineral that is more absorbing at the longer wavelengths (so the reflectance is bluer).

We expect vein-bearing boulders to contain less organic material if their reduced carbon was oxidized by fluids to form the observed carbonates (*66*). Thus, if both a low albedo and near-UV bluing are caused by the carbonization of organics via space weathering, we expect those spectrophotometric effects to be weaker in the vein-bearing rocks—as is observed (Fig. 2A and 2C). Although graphitized carbon could explain the bluing observed in the more recently exposed faces of dark boulders, a UV upturn is also consistent with increasing abundances of magnetite, which has a blue spectral slope shortward of 0.5 μm (*65*).

The presence of potential carbonate veins (*9*) in bright boulders signifies a greater degree of aqueous alteration than in their dark counterparts, suggesting they had an origin within the interior of Bennu's parent body. In dark boulders, we do not find a clear spectral signature indicative of their provenance; however, their textures may provide clues. Brecciated boulders typically have a host-matrix similar in texture to the dark boulders, including examples with clasts of exogenic pyroxene; this implies that these rocks formed near the surface of Bennu's parent body (*38*). Boulders on Bennu thus may have originated from different zones within the parent body. The multi-modal distribution of the boulder populations implies that different processes (or extents of processes), such as aqueous alteration and heating, led to their distinct spectrophotometric properties.

Comparison with Ryugu

Asteroid (162173) Ryugu, visited by the Hayabusa2 spacecraft, is also a low-albedo, carbonaceous near-Earth asteroid. Although both asteroids are thought to have come from primitive asteroid families in the inner main belt (*67*), Ryugu, unlike Bennu, appears to have experienced partial dehydration (*68*). The multi-band cameras onboard the two spacecraft use similar photometric filters in the visible wavelengths, so allow a direct comparison of the spectra from each (*26, 31, 68*). Fig. S13 shows the areal distribution of the reflectance and near-UV to NIR spectral slope of each asteroid. The variation in reflectance on Bennu is 1.7 times that on Ryugu, and Bennu exhibits a bluer overall color. Though the standard deviations of the spectral slope distributions are similar (σ = 0.039 μm^{-1} and 0.034 μm^{-1} for Ryugu and Bennu, respectively), the distribution of color differs spatially. Ryugu shows large-scale latitudinal color differences: The latitudinal difference is ~1/2 the standard deviation of the global color variation (>99% confidence with mean difference of 0.52σ between the redder mid-latitudinal and the bluer equatorial regions (*27*)), which has been attributed to regolith migration from the equator to mid-latitudes during the spin-down of Ryugu (*68*). A latitudinal color trend is also observed on Bennu, but the difference is small compared with its overall color variation (>99% confidence with mean difference of 0.21σ (*31*)). Bennu's slightly bluer equatorial region may indicate the presence of more mature material, which is consistent

with its increasing rotation rate and the associated global patterns of mass movement across the asteroid (*43*).

Unlike Ryugu, color variation on Bennu appears to be dominated by heterogeneity at the meter scale, likely driven by boulders. This suggests that the extent of recent large-scale mass wasting on Bennu may not have been as widespread as the effect of regolith mixing. Episodes of particle ejection have been observed from Bennu's surface (*42*), redistributing its surface material over shorter timescales than those expected for mass wasting (*69*). Large-scale latitudinal spatial patterns may have been obliterated by particle ejection events, which overturns ~10^4 g of surface material per orbit (437 days) (*69*). Of the material lofted, most of the mass (70 to 85%) falls back onto Bennu's surface (*69*).

Young craters on Bennu tend to be redder than the average surface, whereas their young (small) counterparts on Ryugu are bluer than average (*70*). Because Bennu's global photometric spectrum is bluer overall than Ryugu's, the absolute spectral slopes of the craters on the two asteroids are similar (fig. S14). Hayabusa2 NIR observations showed that the freshly exposed interior of the artificial SCI crater on Ryugu does not exhibit a deep hydration band at 2.7 μm (*70*), suggesting that Ryugu's dehydration is not a recent event and likely took place on the parent body (*71*). Although the colors of young craters on Ryugu and Bennu are similar, their hydration properties differ, suggesting that spectral changes in response to space weathering (e.g., bluing versus reddening) can be influenced by initial composition.

Conclusions and prospects for sample return

Bennu's surface is highly diverse, encompassing primitive material potentially from different depths in its parent body (Fig. 7). A smaller proportion consists of exogenic material from another asteroid family delivered in a pre-disruption impact to the parent body (*38*). Although Bennu's low average reflectance (0.044) (*4,10*) is dominated by the abundant dark boulders and particles formed by their breakdown, the limited latitudinal pattern in the observed heterogeneity indicates a well-mixed combination of disparate materials at spatial scales of 1 to 10 m.

Inter-boulder variations in reflectance and texture appear to be primordial in origin, but variations in spectral slopes among craters and between individual rock faces appear to be linked to exposure age (Fig. 7). The young age of small reddish craters and the solar orientation of intra-boulder color patterns indicate that redder spectra are the least recently exposed surfaces. The underlying composition of dark materials on Bennu, which potentially contain a higher proportion of organic material available for carbonization, likely leads to initial near-UV bluing of any freshly exposed redder materials. Initial bluing could also occur with the production of magnetite in response to space weathering. With age, surface materials brighten and become more neutrally sloped, consistent with Bennu's gently blue average spectral slope. This final stage of space weathering may result from accumulations of nanophase and larger metallic iron particles, which potentially have a brightening and reddening effect in low-reflectance and carbonaceous materials (*59*). It could also arise from the development of metal-like optical properties in Bennu surface materials due to progressively stronger carbonization effects, which eventually leads to brightening (*57*).

Our observations suggest that the OSIRIS-REx sample will contain materials with diverse origins and evolution even from a single location on the asteroid. Both the primary and back-up sample sites, Nightingale (56° N, 42° E) and Osprey (11.5° N, 87.5° E), are situated within small reddish craters. The redder colors and shorter 2.7 μm band minimum positions of materials in these craters imply that they are pristine and have experienced less modification from space weathering than the average Bennu surface, and that they potentially have a higher proportion of micron-scale grains.

References and Notes:

1. D. S. Lauretta *et al.*, OSIRIS-REx: sample return from asteroid (101955) Bennu. *Space Science Reviews* **212**, 925-984 (2017).
2. B. E. Clark *et al.*, Asteroid (101955) 1999 RQ36: Spectroscopy from 0.4 to 2.4 μm and meteorite analogs. *Icarus* **216**, 462-475 (2011).
3. Bottke, William F, *et al*. In search of the source of asteroid (101955) Bennu: applications of the stochastic YORP model. *Icarus* **247** (2015): 191-217.
4. D. N. DellaGiustina and J.P Emery, *et al.*, Properties of rubble-pile asteroid (101955) Bennu from OSIRIS-REx imaging and thermal analysis. *Nature Astronomy* **3**, 341 (2019).
5. D. S. Lauretta *et al.*, The unexpected surface of asteroid (101955) Bennu. *Nature* **568**, 55-60 (2019).
6. O. S. Barnouin, *et al.* Shape of (101955) Bennu indicative of a rubble pile with internal stiffness. *Nature Geoscience* **12**, 4 (2019).
7. V. E. Hamilton *et al.*, Evidence for widespread hydrated minerals on asteroid (101955) Bennu. *Nature Astronomy* **3**, 332-340 (2019).
8. A. A. Simon *et al*., The Global Distribution of a 3.4 μm absorption on (101955) Bennu from OSIRIS-REx near IR spectra. *Science* doi: 10.1126/science.abc3522 (2020).
9. H. H. Kaplan *et al*., Bright Carbon-Bearing Veins and Alteration History of (101955) Bennu. *Science* doi: 10.1126/science.abc3557 (2020).
10. C. W. Hergenrother, *et al.,* The operational environment and rotational acceleration of asteroid (101955) Bennu from OSIRIS-REx observations. *Nature communications* **10**, 1 (2019).
11. Saal, E. H. Hauri, J. A. Van Orman, M. J. Rutherford, Hydrogen isotopes in lunar volcanic glasses and melt inclusions reveal a carbonaceous chondrite heritage. *Science* **340**, 1317-1320 (2013).
12. C. R. Chapman, J. W. Salisbury, Comparisons of meteorite and asteroid spectral reflectivities. *Icarus* **19**, 507-522 (1973).
13. D. Nesvorný, *et al.*, Evidence for asteroid space weathering from the Sloan Digital Sky Survey. *Icarus* **173**, 132-152 (2005).
14. M. J. Gaffey *et al.*, Mineralogical variations within the S-type asteroid class. *Icarus* **106**, 573-602 (1993).
15. M. Lazzarin, *et al.*, Space weathering in the main asteroid belt: The big picture. *The Astrophysical Journal Letters* **647**, L179 (2006).

16. H. M. Kaluna, J. R. Masiero, K. J. Meech, Space weathering trends among carbonaceous asteroids. *Icarus* **264**, 62-71 (2016).

17. R. Brunetto, M. J. Loeffler, D. Nesvorný, S. Sasaki, G. Strazzulla, Asteroid surface alteration by space weathering processes. *Asteroids IV* 597-616 (2015).

18. P. Vernazza *et al*., Paucity of Tagish Lake-like parent bodies in the Asteroid Belt and among Jupiter Trojans. *Icarus* **225**, 517-525 (2013).

19. M. Matsuoka *et al.*, Pulse-laser irradiation experiments of Murchison CM2 chondrite for reproducing space weathering on C-type asteroids. *Icarus* **254**, 135-143 (2015).

20. C. Lantz *et al*., Ion irradiation of carbonaceous chondrites: A new view of space weathering on primitive asteroids. *Icarus* **285**, 43-57 (2017).

21. C. Lantz, R. P. Binzel, F. E. DeMeo, Space weathering trends on carbonaceous asteroids: A possible explanation for Bennu's blue slope? *Icarus* **302**, 10-17 (2018).

22. M. S. Thompson *et al.*, The effect of progressive space weathering on the organic and inorganic components of a carbonaceous chondrite. *Icarus* **346**, 113775 (2020).

23. H. M. Kaluna, H. A. Ishii, J. P. Bradley, J. J. Gillis-Davis, P. G. Lucey, Simulated space weathering of Fe-and Mg-rich aqueously altered minerals using pulsed laser irradiation. *Icarus* **292**, 245-258 (2017).

24. M. S. Thompson, *et al.* Spectral and chemical effects of simulated space weathering of the Murchison CM2 carbonaceous chondrite. *Icarus* **319,** 499-511 (2019).

25. D. N. DellaGiustina *et al.*, Overcoming the challenges associated with image-based mapping of small bodies in preparation for the OSIRIS-REx mission to (101955) Bennu. *Earth and Space Science* **5**, 929-949 (2018).

26. B. Rizk *et al.*, OCAMS: the OSIRIS-REx camera suite. *Space Science Reviews* **214**, 26 (2018).

27. B. Zellner, *et al.* The eight-color asteroid survey: Results for 589 minor planets. *Icarus* **61**, 355-416 (1985).

28. F. E. DeMeo, B. Carry, The taxonomic distribution of asteroids from multi-filter all-sky photometric surveys. *Icarus* **226**, 723-741 (2013).

29. D R. Golish, *et al*., Ground and In-Flight Calibration of the OSIRIS-REx Camera Suite. *Space Science Reviews* **216**, 12 (2020).

30. D. R. Golish *et al.*, Disk-resolved photometric modeling and properties of asteroid (101955) Bennu. *Icarus* 113724 (2020). https://doi.org/10.1016/j.icarus.2020.113724

31. Materials and methods are available as supplementary materials.

32. C. A. Bennett *et al*., A high-resolution global basemap of (101955) Bennu. *Icarus* 113690 (2020). https://doi.org/10.1016/j.icarus.2020.113690

33. K. J. Walsh *et al.*, Craters, boulders and regolith of (101955) Bennu indicative of an old and dynamic surface. *Nature Geoscience* **12**, 242-246 (2019).

34. M. G. Daly *et al.*, The OSIRIS-REx laser altimeter (OLA) investigation and instrument. *Space Science Reviews* **212**, 899-924 (2017).

35. O.S. Barnouin *et al.,* Digital terrain mapping by the OSIRIS-REx mission. *Planetary and Space Science.* **180**, 104764 (2020).

36. M. G. Daly. *et al.,* Hemispherical Differences in the Shape and Topography of Asteroid (101955) Bennu. *Science Advances*. doi:10.1126/sciadv.abd3649 (2020).

37. D. C. Reuter *et al.*, The OSIRIS-REx Visible and InfraRed Spectrometer (OVIRS): spectral maps of the asteroid Bennu. *Space Science Reviews* **214**, 54 (2018).

38. D.N. DellaGiustina *et al*., Exogenic Basalt on Asteroid (101955) Bennu. *Nature Astronomy.* doi: 10.1038/s41550-020-1195-z (2020).

39. J.L. Molaro, *et al.* In situ evidence of thermally induced rock breakdown widespread on Bennu's surface. *Nat Commun* **11**, 2913 (2020).

40. C.T. Russell, et al. Dawn at Vesta: Testing the protoplanetary paradigm. *Science* **336,** 684-686 (2012).

41. F. Vilas, A cheaper, faster, better way to detect water of hydration on Solar System bodies. *Icarus* **111**, 456-467 (1994).

42. D. S. Lauretta, *et al*. Episodes of particle ejection from the surface of the active asteroid (101955) Bennu. *Science* **366**, eaay3544 (2019).

43. E. R. Jawin *et al*., Global patterns of mass movement on asteroid (101955) Bennu. *JGR Planets* 125, e2020JE006475 (2020).

44. A. R. Hendrix and F. Vilas. C-complex asteroids: UV-visible spectral characteristics and implications for space weathering effects. *Geophysical Research Letters* **46**, 24 (2019).

45. W. F. Bottke Jr *et al.*, Linking the collisional history of the main asteroid belt to its dynamical excitation and depletion. *Icarus* **179**, 63-94 (2005).

46. S. Marchi *et al.*, The cratering history of asteroid (2867) Steins. *Planetary and Space Science* **58**, 1116-1123 (2010).

47. P. Brown, R. E. Spalding, D. O. ReVelle, E. Tagliaferri, S. P. Worden, The flux of small near-Earth objects colliding with the Earth. *Nature* **420**, 294-296 (2002).

48. A. W. Harris, G. D'Abramo, The population of near-Earth asteroids. *Icarus* **257**, 302-312 (2015).

49. S. Marchi, C. R. Chapman, O. S. Barnouin, J. E. Richardson, J. Vincent, Cratering on asteroids. *Asteroids IV* 725-744 (2015).

50. M. Arakawa *et al.*, An artificial impact on the asteroid 162173 Ryugu formed a crater in the gravity-dominated regime. *Science* **368**, p67 (2020).

51. E. Tatsumi, S. Sugita, Cratering efficiency on coarse-grain targets: Implications for the dynamical evolution of asteroid 25143 Itokawa. *Icarus* **300**, 227-248 (2018).

52. L. P. Keller, E. L. Berger, A transmission electron microscope study of Itokawa regolith grains. *Earth, Planets and Space* **66**, 71 (2014).

53. T. V. Johnson, F. P. Fanale, Optical properties of carbonaceous chondrites and their relationship to asteroids. *Journal of Geophysical Research* **78**, 8507-8518 (1973).

54. Hartzell, C. M. Dynamics of 2D electrostatic dust levitation at asteroids. *Icarus* 333, 234-242 (2019).

55. M. C. Nolan, *et al.* Detection of rotational acceleration of Bennu using HST light curve observations. *Geophysical Research Letters* **46**, 4 (2019).

56. W. F. Bottke, *et al.* Meteoroid Impacts as a Source of Bennu's Particle Ejection Events. *Journal of Geophysical Research: Planets* **125**, e2019JE006282 (2020).

57. L. Moroz *et al.*, Optical alteration of complex organics induced by ion irradiation: 1. Laboratory experiments suggest unusual space weathering trend. *Icarus* **170**, 214-228 (2004).

58. B. Hapke, Space weathering from Mercury to the asteroid belt. *Journal of Geophysical Research: Planets* **106**, 10039-10073 (2001).

59. A. S. Rivkin, E.S. Howell, F. Vilas, L.A. Lebofsky, Hydrated Minerals on Asteroids: The Astronomical Record. *Asteroids III* **1**, 235-253 (2002).

60. B. Rozitis *et al.*, Asteroid (101955) Bennu's Weak Boulders and Thermally Anomalous Equator. *Science Advances* doi:10.1126/sciadv.abd3649 (2020).

61. C. A. Johnson, M. Prinz, Carbonate compositions in CM and CI chondrites and implications for aqueous alteration. *Geochimica et Cosmochimica Acta.* 57, 2843-2852 (1993).

62. Morlok, A., Bischoff, A., Stephan, T., Floss, C., Zinner, E., & Jessberger, E. K. Brecciation and chemical heterogeneities of CI chondrites. *Geochimica et Cosmochimica Acta* 70, 5371-5394 (2006).

63. Alfing, J., Patzek, M., & Bischoff, A. Modal abundances of coarse-grained (> 5 μm) components within CI-chondrites and their individual clasts–Mixing of various lithologies on the CI parent body (ies). *Geochemistry* 79, 125532 (2019).

64. E. A. Cloutis, *et al.*, Spectral reflectance properties of HED meteorites CM2 carbonaceous chondrites: Comparison to HED grain size and compositional variations and implications for the nature of low-albedo features on Asteroid 4 Vesta. *Icarus* 223, 850-877 (2013)

65. M. R. Izawa, *et al.*, Spectral reflectance properties of magnetites: Implications for remote sensing. *Icarus* 319, 525-539 (2019).

66. C. M. Alexander., *et al.* Carbonate abundances and isotopic compositions in chondrites. *Meteoritics & Planetary Science* 50, 810-833 (2015).

67. J. De León, *et al.* Expected spectral characteristics of (101955) Bennu and (162173) Ryugu, targets of the OSIRIS-REx and Hayabusa2 missions. *Icarus* 313, 25-37 (2018).

68. S. Sugita, *et al.*, The geomorphology, color, and thermal properties of Ryugu: Implications for parent-body processes. *Science* 364, eaaw0422 (2019).

69. C. W. Hergenrother *et al.*, Photometry of particles ejected from active asteroid (101955) Bennu. *Journal of Geophysical Research: Planets* 125, e2020JE006381 (2020).

70. T. Morota, *et al.,* "Sample collection from asteroid (162173) Ryugu by Hayabusa2: Implications for surface evolution." Science 368 (2020): 654-659.

71. K. Kitazato, *et al.*, Asteroid 162173 Ryugu: Surface composition as observed by Hayabusa2/NIRS3, 13, EPSC-DPS2019-1376-1, 2019.

72. J.Y. Li, *et al.* Asteroid photometry. *Asteroids IV,* 129-150(2015).

73. L. Keszthelyi, *et al.* Support and future vision for the integrated software for imagers and spectrometers (ISIS). *Lunar and Planetary Science Conference* 44 (2013).

74. Principal component analysis of raw data. https://www.mathworks.com/help/stats/pca.html

75. Scrucca L, Fop M, Murphy TB, Raftery AE (2016). "mclust 5: clustering, classification and density estimation using Gaussian finite mixture models." The R Journal, 8(1), 289–317. https://doi.org/10.32614/RJ-2016-021.

76. S.J. Bus and R. P. Binzel. Phase II of the small main-belt asteroid spectroscopic survey: A feature-based taxonomy. Icarus 158, 146-177 (2002).

77. C. M. Ernst, *et al.* The Small Body Mapping Tool (SBMT) for accessing, visualizing, and analyzing spacecraft data in three dimensions. *Lunar and Planetary Science Conference* 49 (2018).

78. W. F. Bottke, et al. Velocity distributions among colliding asteroids. Icarus 107, 255-268 (1994).

79. E. Tatsumi, *et al.* Updated inflight calibration of Hayabusa2's optical navigation camera (ONC) for scientific observations during the cruise phase. *Icarus* 325, 153-195 (2019).

80. Browning, L.B., H.Y. McSween Jr., and M.E. Zolensky (1993) Correlated alteration effects in CM carbonaceous chondrites. Geochimica et Cosmochimica Acta, 60, 2621-2633.

81. Buseck, P.R., and X. Hua (1993) Matrices of carbonaceous chondrite meteorites. Annual Reviews of Earth and Planetary Science, 21, 255-305.

82. Zolensky M. E., R.A. Barrett, and L. Browning (1993) Mineralogy and composition of matrix and chondrule rims in carbonaceous chondrites. Geochimica et Cosmochimica Acta 57, 3123-3148.

83. Howard, K.T., G.K. Benedix, P.A. Bland, and G. Cressey (2011) Modal mineralogy of CM chondrites by X-ray diffraction (PSD-XRD): Part 2. Degree, nature and settings of aqueous alteration. Geochimica et Cosmochimica Acta, 75, 2735-2751.

84. Cloutis, E.A., M.J. Gaffey, and T.F. Moslow (1994) Spectral reflectance properties of carbon-bearing materials. Icarus, 107, 276-287.

85. Cloutis, E.A., T. Hiroi, M.J. Gaffey, C.M.O'D. Alexander, and P. Mann (2011a) Spectral reflectance properties of carbonaceous chondrites: 1. CI chondrites. Icarus, 212, 180-209.

86. Cloutis, E.A., P. Hudon, T. Hiroi, M.J. Gaffey, and P. Mann (2011b) Spectral reflectance properties of carbonaceous chondrites: 2. CM chondrites. Icarus, 216, 309-346.

87. Pearson, V.K., M. A. Sephton, I. A. Franchi, J. M. Gibson, and I. Gilmour (2006) Carbon and nitrogen in carbonaceous chondrites: Elemental abundances and stable isotopic compositions. Meteoritics and Planetary Science, 41, 1899-1918.

88. Hildebrand, A.R., L. Hanton, M. Rankin, and M.I. Ibrahim (2015) An asteroid regolith simulant for hydrated carbonaceous chondrite lithologies (HCCL-1). 78th Meteoritical Society Meeting; abstract #5368.

89. Croat, T.K., T. Bernatowicz, S. Amari, S. Messenger, and F.J. Stadermann (2003) Structural, chemical, and isotopic microanalytical investigations of graphite from supernovae. Geochimica et Cosmochimica Acta, 67, 4705-4725.

90. Amari, C.E., M.-C. Maurel, G. Sagon, and M.-H. Baron (2005) The micro-distribution of carbonaceous matter in the Murchison meteorite as investigated by Raman imaging. Spectrochimica Acta A, 61, 2049-2056.

Acknowledgments: We thank the entire OSIRIS-REx Team for making the encounter with Bennu possible. For fig. S5, we thank D. Rachford and IMV Minerals for providing the SAP105 sample, and S. Mertzman of Franklin and Marshall College for confirming the composition of the SAP105 sample. We thank Robert J. Burmeister for assistance with graphic design of the figures. **Funding:** D.N.D, K.N.B., K.J.W., P.H.S., D.R.G., E.B.B., R.L.B., T.B., H.C., B.E.C., A.S., K.B., C.A.B., W.F.B., J.I.B., H.C.C., C.Y.D.D., K.L.E., V.E.H. C.W.H., E.S.H., E.R.J., H.H.K., L.L.C., L.L., J.Y.L., M.C.N, J.N., N.A.P., B.Ri, A.J.R., N.K.S., A.A.S., C.W.V.W., and D.S.L. were supported by NASA under Contract NNM10AA11C issued through the New Frontiers Program. J.L.M. and D.T. were supported by the NASA OSIRIS-REx Participating Scientist Program 80NSCC18K0230. A.R.H. was supported by the NASA Solar System Exploration Research Virtual Institute 2016 (SSERVI16) Cooperative Agreement TREX NNH16ZDA001N. E.T., K.Y., and S.S. were supported by the Japanese Society for Promotion of Science (JSPS) Core-to-Core program "International Planetary Network". The OLA instrument and funding for M.G.D. and M.M.A.A and support for A.P., E.A.C., and D.M.A was provided by the Canadian Space Agency. J.L.R., E.T., M.Po,. and J.d.L. acknowledge support from the project AYA2017-89090-P of the Spanish MINECO and from the project ProID2017010112 under the OP-ERDF-ESF and the Canarian Agency for Research, Innovation and Information Society (ACIISI). M.Pa. was supported by the Italian Space Agency (ASI) under the ASI-INAF agreement no. 2017-37-H.0. C.A., J.D.P.D., M.A.B, M.D., P.H.H., P.M., and S.F. acknowledge support from the French space agency CNES. P.M. also acknowledges support from the European Union's Horizon 2020 research and innovation program under grant agreement No 870377 (project NEO-MAPP). C.A. was also supported by the French National Research Agency under the project "Investissements d'Avenir" UCAJEDI (ANR-15-IDEX-01). C.A. and M.D. also acknowledge support from the ANR "ORIGINS" (ANR-18-CE31-0014). B.Ro. acknowledges support from the Royal Astronomical Society (RAS) and the UK Science and Technology Facilities Council (STFC). **Author contributions:** D.N.D., P.H.S., D.R.G., B.Ri., and C.Y.D.D. planned and calibrated OCAMS MapCam and PolyCam observations of Bennu. D.N.D., K.N.B., P.H.S., D.R.G., T.L.B, K.J.B., C.A.B., J.I.B., K.L.E., L.L.C., and N.K.S. created MapCam color parameter maps of Bennu. K.N.B., E.B.B., J.N., D.T., and R.B.V.A. mapped craters and boulders on Bennu. D.N.D., K.N.B., K.J.W., P.H.S., E.B.B., R.-L.B, M.M.A.A., and W.F.B.. performed the statistical analysis of boulder and craters colors. E.T., K.Y., and S.S. performed comparisons of the colors of Bennu and Ryugu. E.A.C., B.E.C., A.R.H., A.S., D.M.A., and A.P. performed comparisons between Bennu colors and laboratory spectra. J.D.P.D., A.A.S., H.H.K., and V.E.H. processed and interpreted OVIRS observations of Bennu. M.G.D., M.M.A.A., R.-L.B, and N.A.P. processed and interpreted OLA observations of Bennu. D.N.D., P.H.S., D.R.G., K.J.W., R.-L.B., H.C., C.A., M.A.B., H.C.C.Jr., M.D., J.d.L., S.F., V.E.H., P.H.H., C.W.H., E.S.H., E.R.J., H.H.K., L.F.L., J.Y.L., P.M., J.L.M., M.C.N., M.Pa., M.Po., A.J.R., B.Ro., A.A.S., D.T., and C.W.V.W. contributed to the conceptualization and writing. D.S.L. contributed to the conceptualization and leads the OSIRIS-REx mission. **Competing interests:** We declare no competing interests. **Data and materials availability:** Full-resolution MapCam color maps of Bennu, as shown in Fig. 1 and fig. S5, are available at 10.6084/m9.figshare.12996494. Catalogues of the boulders and craters we used are available as Data S1 and S2 respectively. The stereophotoclinometry v28 and OLA v20 shape models of Bennu are available through the Small Body Mapping Tool at http://sbmt.jhuapl.edu/. Detailed Survey OCAMS (MapCam and PolyCam), Orbital B OLA, and Detailed Survey and Recon A OVIRS data are available via the Planetary Data System (PDS) at:

https://sbnarchive.psi.edu/pds4/orex/orex.ocams/data_calibrated/detailed_survey/, https://sbnarchive.psi.edu/pds4/orex/orex.ocams/data_calibrated/recon/, https://sbnarchive.psi.edu/pds4/orex/orex.ola/data_calibrated/orbit_b/, https://sbnarchive.psi.edu/pds4/orex/orex.ovirs/data_calibrated/detailed_survey/ and https://sbnarchive.psi.edu/pds4/orex/certified/orex.ovirs/data_calibrated/recon/, respectively. The list of MapCam images used to produce the maps in Fig. 1 is available as Data S3.

Supplementary Materials:

Materials and Methods

Figs. S1 to S16

Tables S1 and S2

References (*72-90*)

Data S1-S3

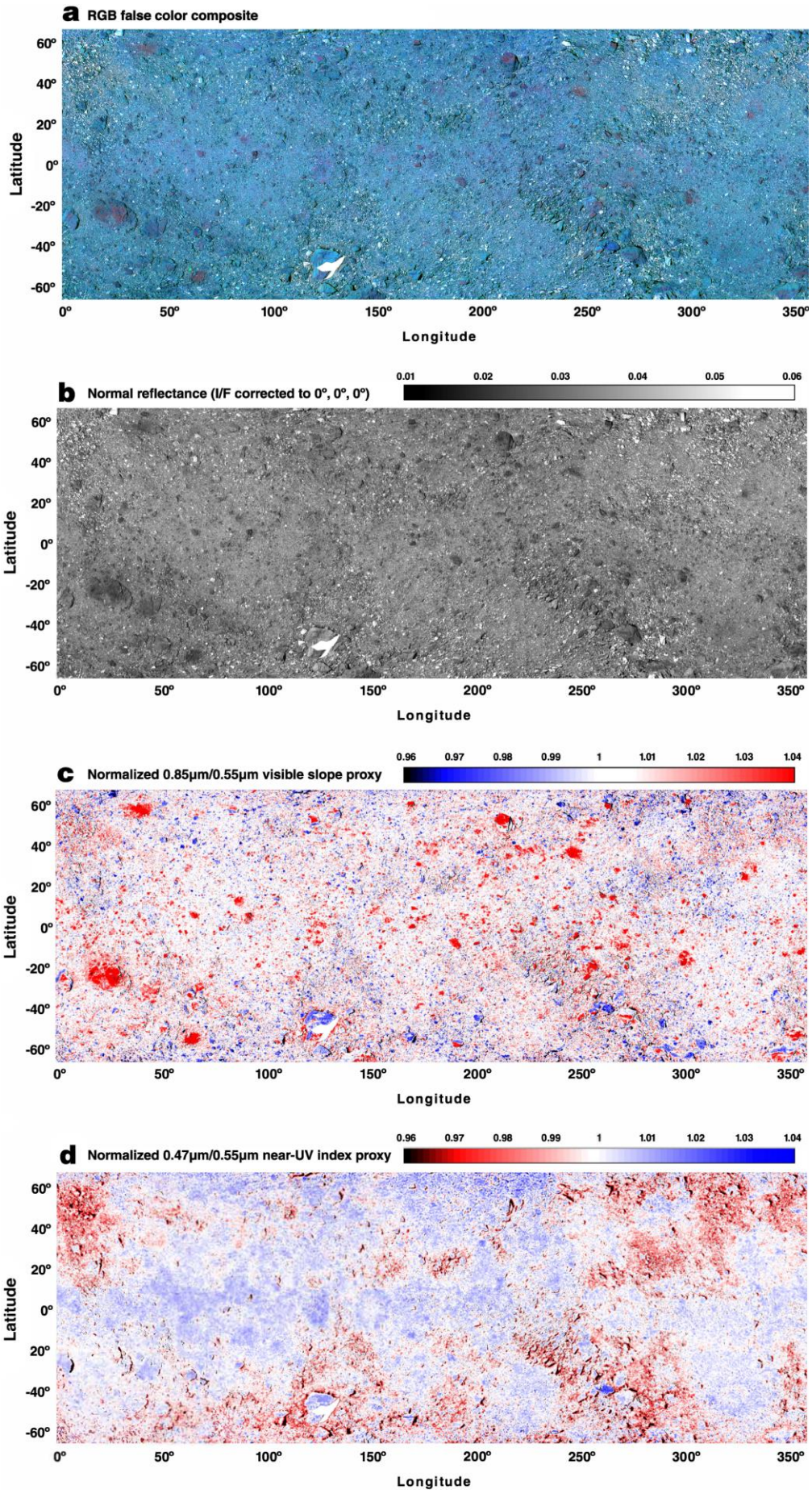
a RGB false color composite
b Normal reflectance (I/F corrected to 0°, 0°, 0°)
0.01 0.02 0.03 0.04 0.05 0.06
c Normalized 0.85μm/0.55μm visible slope proxy
0.96 0.97 0.98 0.99 1 1.01 1.02 1.03 1.04
d Normalized 0.47μm/0.55μm near-UV index proxy
0.96 0.97 0.98 0.99 1 1.01 1.02 1.03 1.04
Latitude
60° 40° 20° 0° -20° -40° -60°
Longitude
0° 50° 100° 150° 200° 250° 300° 350°

Fig. 1. Color composite, reflectance, and band ratio maps of Bennu. (**A**) False-color Red-Green-Blue color model (RGB) composite overlaid on a 0.55-μm (*v* band) normal reflectance map of Bennu. Color channels are: red, *x*/*v* (0.85/0.70 μm, mid-VIS to NIR spectral slope); green, w-band strength (depth at 0.70 μm, composition, fig. S5); and blue, *b*′/*v* (0.47/0.55 μm, near-UV slope). (**B**) Normal reflectance. (**C**) The *x*/*v* band ratio, a proxy for the mid-VIS to NIR spectral slope, where warmer values correspond to redder spectral slopes; values >1 are redder than the global average, and values <1 are less red than the global average. (**D**) The *b*′/*v* band ratio, a proxy for the near-UV slope, where higher values correspond to bluer spectral slopes; values >1 are bluer than the global average, and values <1 are less blue than the global average. All maps range from 65°N to 65°S latitude, 0–360°E longitude.

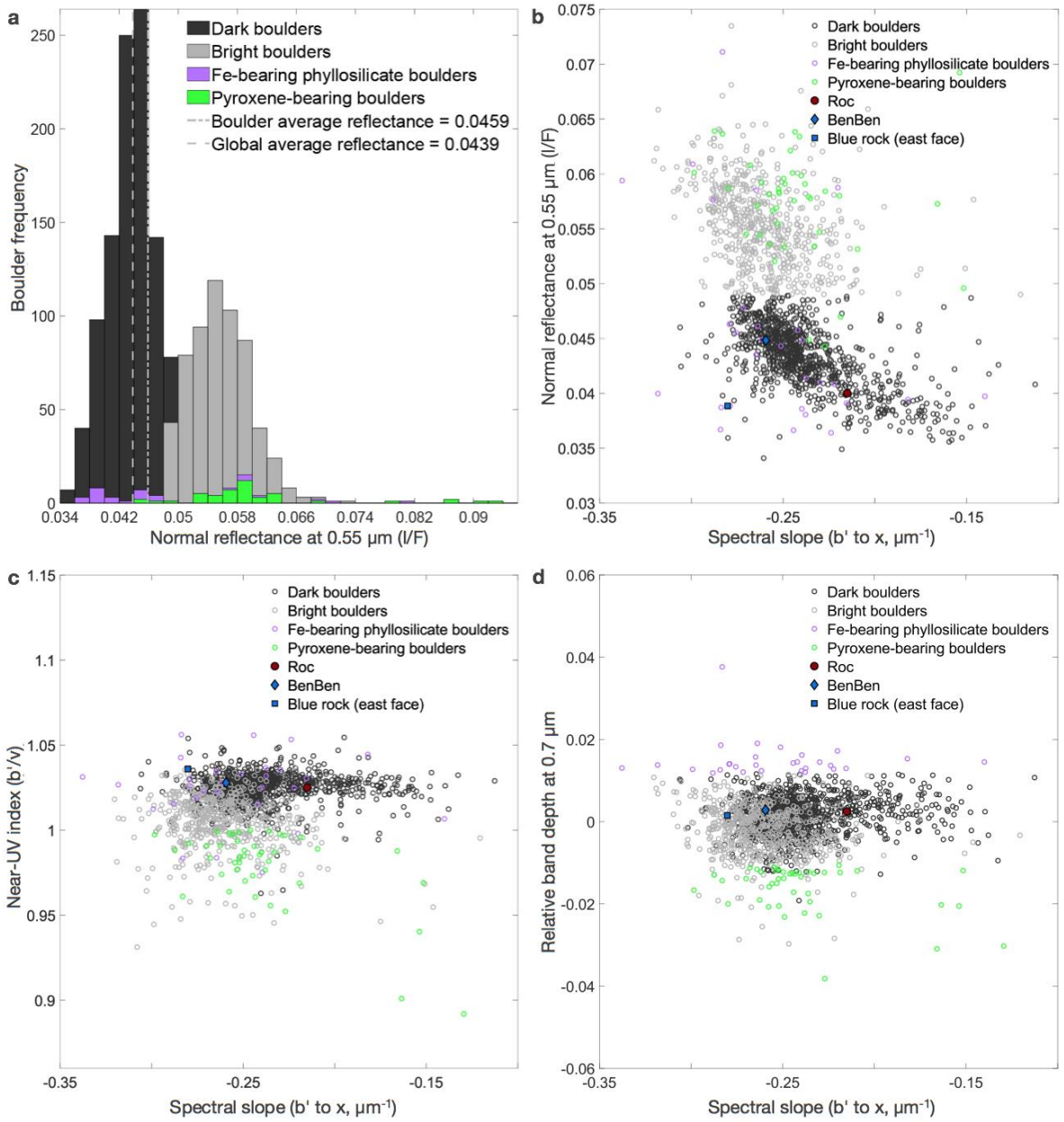

Fig. 2. Variation of boulder color and reflectance on Bennu. (**A**) Reflectance distribution of boulders (>5 m) on Bennu. The distribution is multi-modal with more than one Gaussian component (*31*). Shading and colors indicate different classifications of boulders, as indicated in the legend. (**B**) Normal reflectance versus absolute spectral slope of the same boulder populations; some individual boulders are indicated in the legend. Dark boulders tend to be redder, and their reflectance monotonically decreases with increasing (redder) spectral slopes, whereas bright boulders are bluer and more scattered (*31*). (**C**) The near-UV index (b'/v band ratio) versus the b' to x spectral slope. Dark boulders tend to have a steeper near-UV slope relative to the global average (>1), whereas bright boulders are more often spectrally flat or show a downturn in the near-UV (from the b' to v bands). (**D**) The relative band depth at 0.7 μm (w band) versus the b' to x spectral slope. Some boulders show an absorption feature at 0.7 μm (relative w band depth >0), indicative of Fe-bearing phyllosilicates. The boulders named Roc (23.6°S, 25.3°E; Fig. 3C) and

BenBen (46.8°S, 127.5°E) are two of the largest on Bennu; both are dark. The blue rock (39.80°S, 263.02°E) is shown in Fig. 3E.

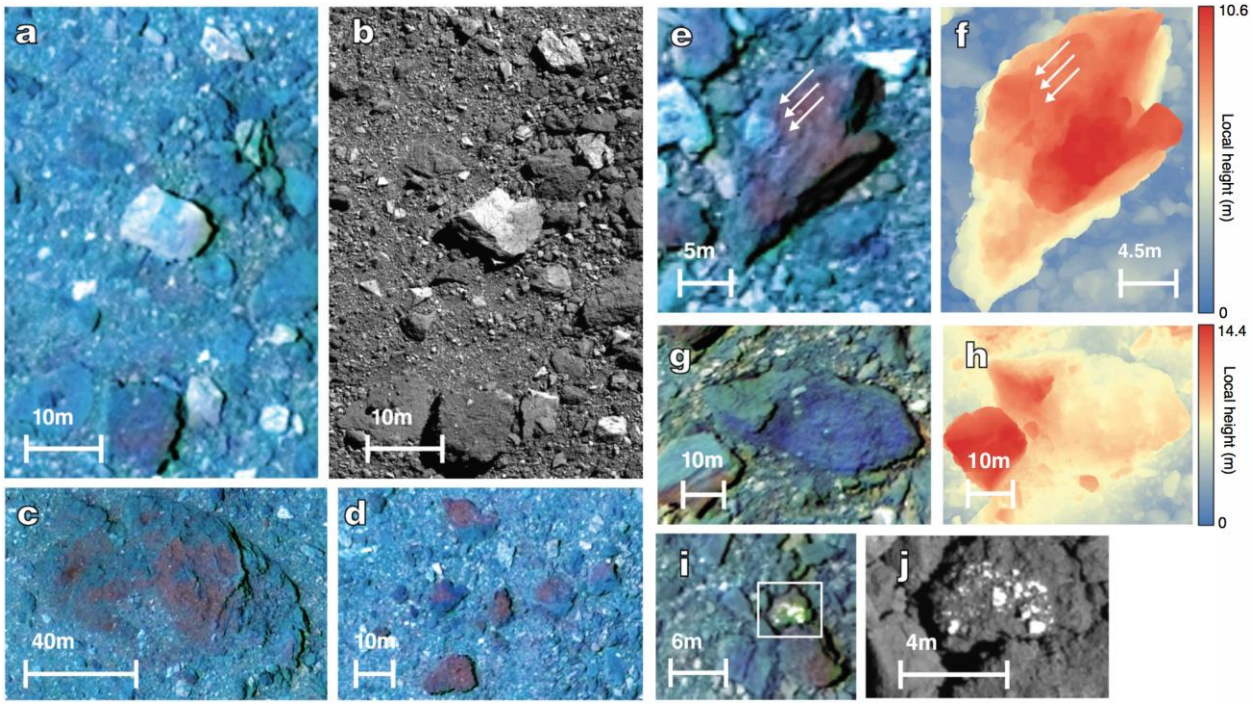

Fig. 3. Examples of boulder color and morphology. All RGB color composite images are shown on the same color scale as Fig. 1A. Bright boulders near 17.76°S, 74.74°E in (**A**) MapCam (25 cm pixel^{-1}) and (**B**) PolyCam (5.25 cm pixel^{-1}) images, indicated by white arrows. The higher-resolution panchromatic PolyCam image (B) shows the angular morphology of bright boulders. Dark boulders near (**C**) 23.6°S, 25.3°E; and (**D**) 3.92°N, 178.98°E, some of which display intra-boulder color variation. This includes Roc (C), which is the largest boulder observed on Benn at ~100 m in the longest observable dimension. (**E**) A dark boulder with resolvable clasts that appear distinct from the host matrix (4.62°S, 248.95°E). (**F**) Digital terrain model of the same boulder. The three arrows highlight the same clast in both panels. (**G**) A rock at 39.80°S, 263.02°E. The darker and bluer portion corresponds to a lower-relief fractured face in the digital terrain model (**H**) (**I**) A boulder that appears to contain clasts and be brecciated; the bright clasts with a greenish color signature are indicative of pyroxene in this false color scale (J) a higher-resolution PolyCam image (5.25 cm pixel^{-1}) of the same boulder. A wider context image is shown in fig. S15.

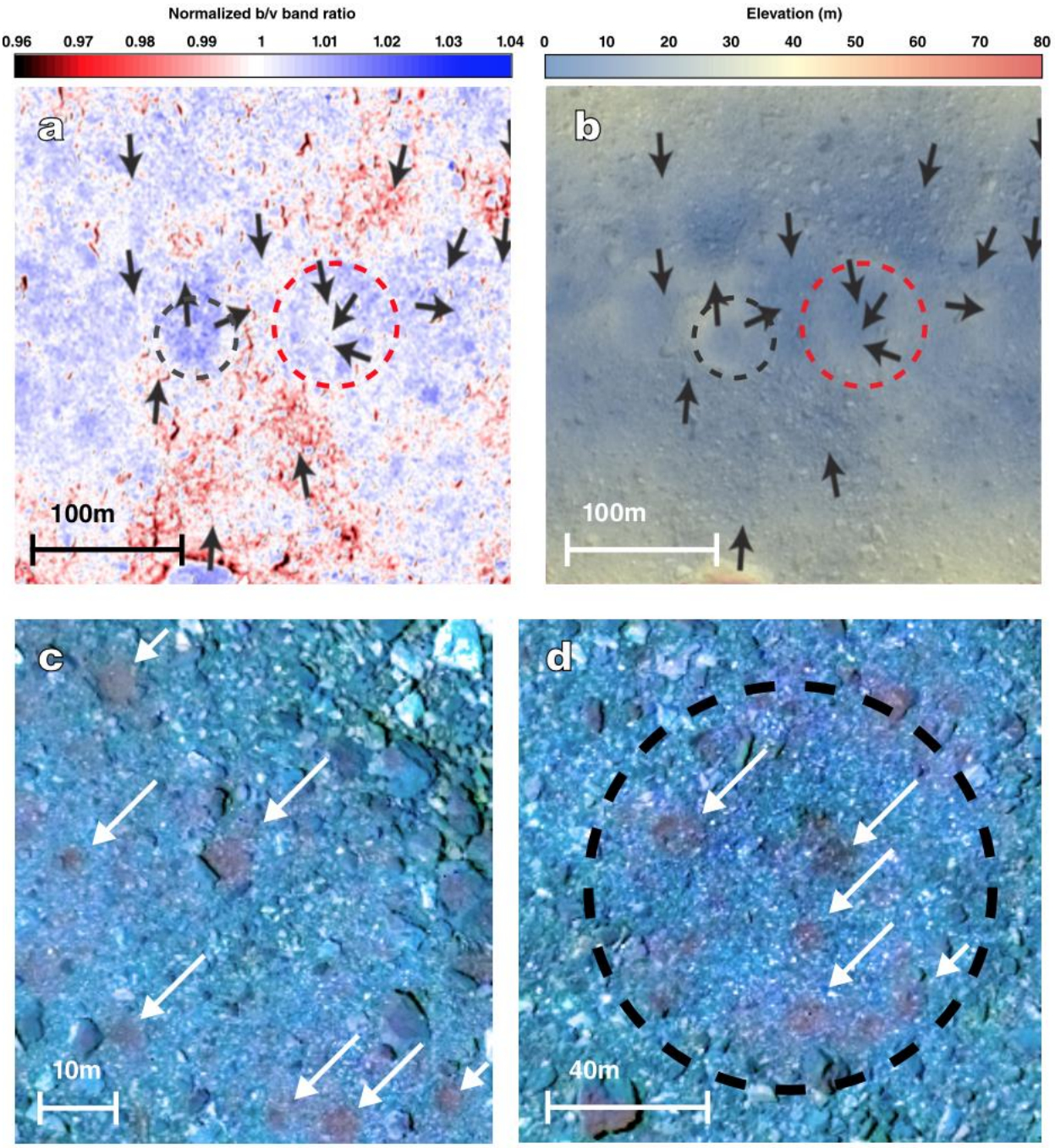

Fig. 4. Examples of crater color. (**A**) The *b′/v* band ratio map of equatorial craters at 3.05°S, 128.79°E (black dashed line) and 1.06°S, 152.75°E (red dashed line), which have a higher near-UV index and are considered blue units. (**B**) An elevation map of the same equatorial craters in (A). These blue units correspond with areas that show recent indications of mass movement away from regionally high elevations, such as from crater rims. Black arrows correspond locations of previously mapped mass movement (*43*). (**C** and **D**) RGB color composites images of small craters (indicated by white arrows), shown on the same color scale as Fig. 1A. As indicated by their color, these craters are consistently redder than Bennu's average terrain, with positive to slightly blue *b′* to *x* spectral slopes. The blue crater indicated by the dashed black line in (A), (B), and (D) has been overprinted by several smaller reddish craters.

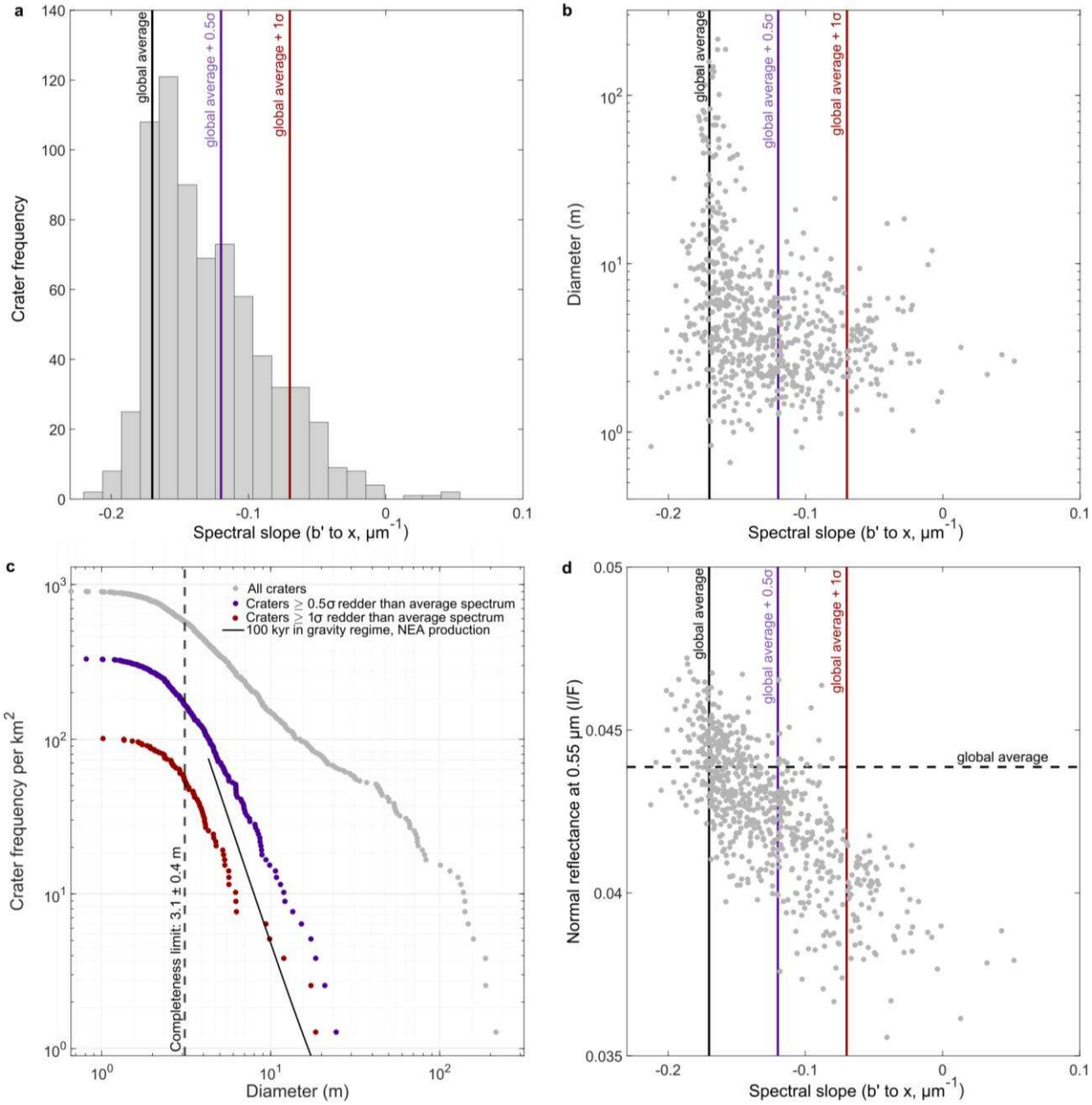

Fig 5. Color, reflectance, and size distribution of Bennu's craters. (**A**) The *b′* to *x* spectral slope distribution of craters on Bennu, which are not normally distributed. (**B**) Crater diameter as a function of the crater's median *b′* to *x* spectral slope. Craters have more negative spectral slopes at higher size and frequency; this suggests that redder (more positively sloped) craters are younger. (**C**) The crater size frequency distribution on Bennu for craters classified on the basis of their *b′* to *x* spectral slopes. The black line shows the expected crater production for 100,000 years in near-Earth space (cumulative power-law index of –2.7), assuming cratering in the gravity regime (*51*). The size-frequency distribution of the reddish craters (purple circles) is more consistent with the black line at small diameters than that of the global crater population (gray circles). The reddest subset of these craters (red circles) fall below the black line, and appear to have formed more recently than 100,000 years ago. (**D**) The normal reflectance of craters on Bennu as a function of *b′* to *x* spectral slope. Like dark boulders, the reflectance of craters monotonically decreases with

increasing (redder) spectral slopes (*31*). Supporting information for the relationship between spectral slope and crater size and frequency is shown in fig. S16.

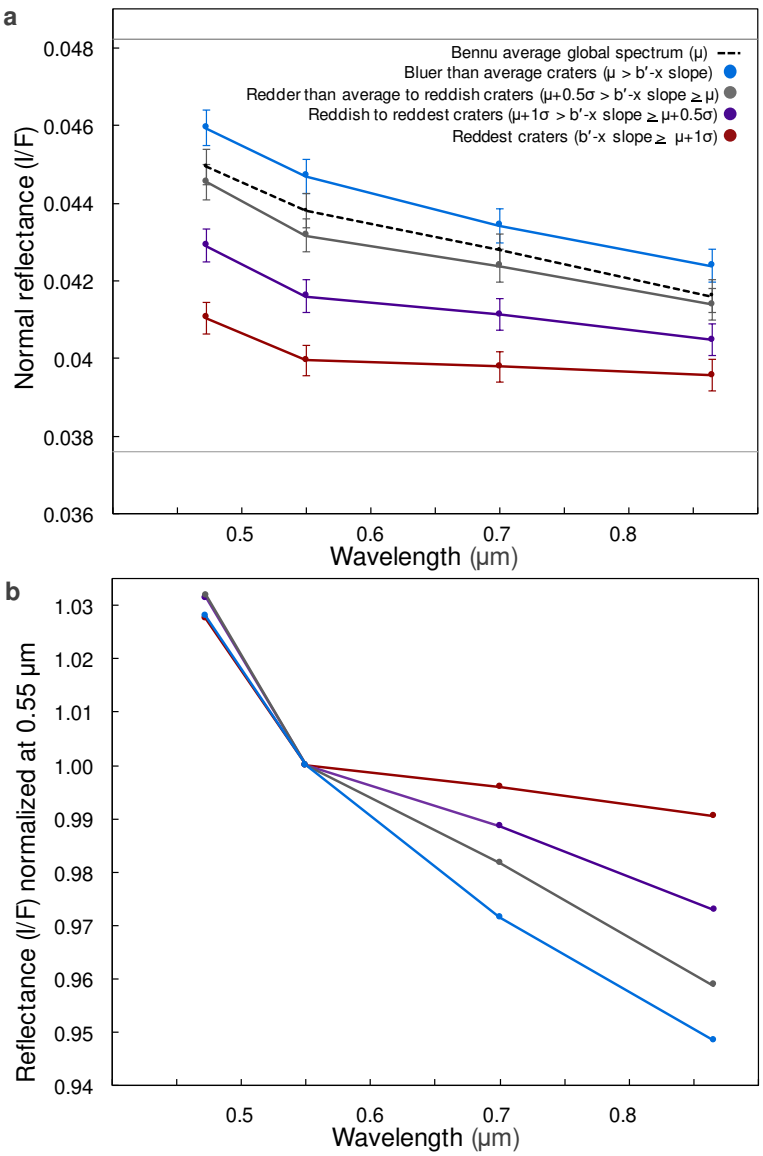

Fig. 6. The evolution of crater colors from MapCam data. Older craters have bluer overall spectra from *b′* to *x* (Fig. 5); here we show variations in each filter separately. (**A**) The average absolute reflectance spectra of all craters within a given *b′* to *x* slope range (see Fig. 5A). The light gray box encompasses the range of absolute radiometric uncertainty (*29*), while error bars show the relative precision of OCAMS measurements (*26*). Craters become brighter as their spectral slopes steepen. (**B**) The same reflectance spectra shown in (A), normalized at 0.55 μm. The progression from the mid-VIS to NIR (*v* to *x* bands) dominates the evolution of crater spectra, which mature toward more negative slopes. In the near-UV, spectra with intermediate *b′* to *x* slopes steepen (*31*). This may result from more rapid brightening in the near-UV relative to longer wavelengths, a deepening of absorption feature at 0.55 μm (*v* band), or both. As a result, crater spectra show a non-unidirectional change near the *b′* band as they age.

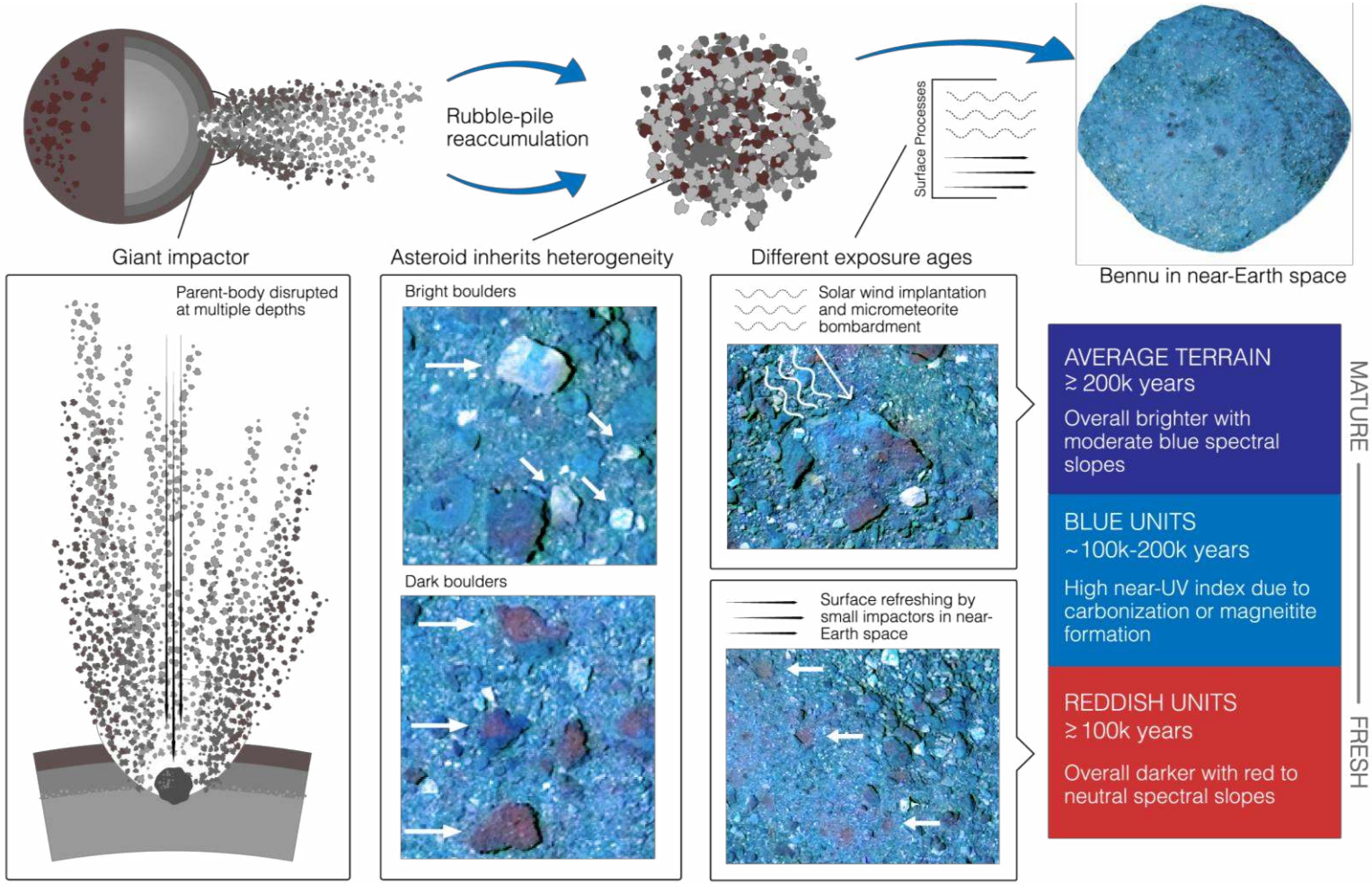

Fig 7. Proposed model of color and reflectance diversity. We propose that distinct rock types formed at different depths on Bennu's parent body. After the parent body was catastrophically disrupted by a giant impactor, Bennu accumulated from its debris (*4-6*) and inherited these distinct materials, leading to the observed heterogeneity among boulders on Bennu. Since Bennu's formation and subsequent transit to near-Earth space, it has been altered by exposure to the space environment, which ultimately results in its moderately blue global color. Small near-Earth impactors also continually refresh the surface, creating craters of comparatively fresh, reddish material, which weather towards bluer colors on a timescale of ~10^5 years.

Table 1. Adopted color units on Bennu and their distinguishing properties.

Color Unit	Distinguishing Properties
Bright boulders	Normal reflectance from 0.049 to 0.074. Bluish spectral slopes slightly steeper than the global average in the mid-VIS to NIR wavelengths (0.52 to 0.96 μm) but often spectrally flat or show a downturn in the near-UV wavelengths (0.44 to 0.50 μm; MapCam *b′* band). Diameters <10 m.
Dark boulders	Normal reflectance from 0.034 to 0.049, overlapping with the average reflectance of Bennu (0.044). Slopes tend to be redder in the mid-VIS to NIR wavelengths (0.52 to 0.96 μm) and often show an upturn in the near-UV wavelengths consistent with the global average. Diameters range from decimeters to 95 m.
Fe-bearing phyllosilicate boulders	Absorption feature at 0.70 μm (determined from a relative band depth >1% in the MapCam *w* band). Wide range of reflectance, most often overlapping with the dark boulders.
Pyroxene-bearing boulders	Absorption feature beyond 0.89 μm (determined from a downturn in the MapCam *x* band relative to the *w* band) due to pyroxene (*36*). Reflectance up to 0.26 (*36*). Can occur as discrete boulders or pyroxene-bearing clasts in a dark boulder–like matrix.
Blue units	Boulders and craters showing an upturn in the near-UV wavelengths that exceeds that of the global average photometric spectrum, possibly resulting from an absorption at 0.55 μm.
Reddish craters	Small (<25 m diameter) craters that are ≥0.5σ redder than Bennu's global average (median) and contain material that is not resolved at ~2 cm pixel^{-1}.
Breccias	Medium (~5 m) to large (>10 m) boulders with embedded clasts (tens of centimeters) whose spectrophotometric properties are distinct from the host matrix, which resembles the dark boulders.
Average terrain	Areas absent of large boulders (≳20 m) that have a photometric spectrum similar to the global average (median).

Science
AAAS

Supplementary Materials for

Variations in Color and Reflectance on the Surface of Asteroid (101955) Bennu

D.N. DellaGiustina, K.N. Burke, K.J. Walsh, P.H. Smith, D.R. Golish, E.B. Bierhaus, R.-L. Ballouz, T. L. Becker, H. Campins, E. Tatsumi,, K. Yumoto, S. Sugita, J.D. Prasanna Deshapriya, E.A. Cloutis, B.E. Clark, A.R. Hendrix, A. Sen, M. M. Al Asad, M.G. Daly, D.M. Applin, C. Avdellidou, M.A. Barucci, K. J. Becker, C.A. Bennett, W.F. Bottke, J.I. Brodbeck, H.C. Connolly Jr., M. Delbo, J. de Leon, C.Y. Drouet d'Aubigny, K.L. Edmundson, S. Fornasier,, V.E. Hamilton, P.H. Hasselmann, C.W. Hergenrother, E.S. Howell, E.R. Jawin, H.H. Kaplan, L. Le Corre, L. F. Lim, J.Y. Li, P. Michel, J.L. Molaro, M.C. Nolan, J. Nolau, M. Pajola, A. Parkinson, M. Popescu,, N.A. Porter, B. Rizk, J.L. Rizos, A. J. Ryan, B. Rozitis, N. K. Shultz, A.A. Simon, D. Trang, R.B. Van Auken, C.W.V. Wolner , and D.S. Lauretta

Correspondence to: danidg@lpl.arizona.edu

This PDF file includes:

Materials and Methods

1. Image acquisition and calibration

PolyCam images were acquired under varying imaging conditions in the Detailed Survey mission phase (***Error! Reference source not found.***,***Error! Reference source not found.***), and MapCam images were collected on 14 March 2019 (Baseball Diamond Flyby 2) and 26 September 2019 (Baseball Diamond Flyby 2b). OCAMS images were radiometrically calibrated, corrected for charge smear, and converted into units of reflectance (*I/F* or radiance factor) using previously described techniques (***Error! Reference source not found.***). Calibrated OCAMS data have a 5% absolute radiometric uncertainty and a 1% relative uncertainty (**Error! Reference source not found.**). PolyCam images were used only for geologic context so were not photometrically corrected. MapCam images were photometrically corrected to solar phase (α), incidence (i), and emission (e) angles of 0°. Correcting (i, e, α) to 0°,0°,0° converts the reflectance data into a measure of normal reflectance (**Error! Reference source not found.**). Photometric correction used a Lommel-Seeliger disk function and the Robotic Lunar Observatory (ROLO) phase function (***Error! Reference source not found.***). The ROLO model is preferred for correction to 0° phase because it accounts for Bennu's small opposition surge (***Error! Reference source not found.***), which is slightly stronger in the *b′* band (versus the other photometric filters). The accuracy of the correction is dominated by the accuracy of the global 3D tessellated digital terrain model (DTM) used to calculate the photometric angles and the registration of the images to that shape model. We used an OLA-based shape model (v20) with a 20 cm facet size for photometric correction (***Error! Reference source not found.***).

2. Image mosaicking and photogrammetric control

Image mosaicking was performed using a version of ISIS3 (***Error! Reference source not found.***) modified to support processing with tessellated 3D shape models. Precise co-alignment between different filter images is imperative for spectral analysis. It is assumed that color images are acquired in sets where each filter is taken in some consecutive order and as close in time as possible. To achieve color registration of MapCam images, the photogrammetric control process is performed in two stages.

The first stage is focused on spatial registration between overlapping images and accurate alignment with a DTM; we used the 80 cm mean facet size v28 shape model of Bennu by updating the existing model (***Error! Reference source not found.***) using stereophotoclinometric techniques. The initial image control network was created with a single MapCam filter and exposure time; we used the *v* band (0.55 μm) at the longest exposure time (18.29 ms). Long exposures have the highest single-to-noise ratio for images of Bennu's dark surface materials but can saturate very bright features. We discarded saturated pixels in our analysis. The photogrammetric control process involved global registration of all *v* band filter images, and used OCAMS image mosaicking procedures described elsewhere (***Error! Reference source not found.***, ***Error! Reference source not found.***). The adjusted camera pointing for each individual *v* band image after bundle adjustment resulted in an improvement in the registration between overlapping images and the registration between images and the modeled terrain of Bennu. The improvement was evaluated by creating a basemap with the corrected *v* band images and comparing it with a shaded relief of the DTM.

The second stage involved creating individual color sets by pairing each corrected *v* band image with a corresponding remaining filter acquired close in time. The photogrammetric control procedure involves adjusting the camera pointing of the remaining filters within a color set directly to the corresponding newly adjusted *v* band image. This process ensures that the camera pointing of each remaining filter image matches that of the *v* band. The end results are maps in each MapCam band (*b′, v, w, x*) and span 0–360° longitude and ±65° latitude.

To create color cubes, we performed subpixel image-to-ground and image-to-image registrations. The *b′/v* ratio (0.47 μm/0.55 μm) represents the near-UV index. The *x/v* ratio (0.86 μm/0.55 μm) represents the mid-VIS to NIR slope. We also calculated the relative band depth of the *v* (0.55 μm) and *w* (0.7 μm) bands using an equation for relative band depth (***Error! Reference source not found.***). Band ratio maps were normalized against Bennu's median global values, and therefore emphasize variation from the average. We applied a 7 × 7 boxcar lowpass filter combination to reduce speckle noise in the band ratio cubes. Stray light was also reduced using a cube-to-cube normalization procedure for the *w* (0.7 μm) relative band map.

3. Principal component analysis of color mosaics

We performed a principle component analysis (PCA) on the color data to identify the maximum variance of spectra from Bennu. We used MATLAB's built-in PCA functionality (***Error! Reference source not found.***), which returns the principle component (PC) scores for each pixel, mapped into the first, second, and third components. Subsequently, we identified spectral features by selecting portions of the histogram of each PC and calculating the average spectrum of the pixels that fell within the high and low ranges of the PC, as determined by examining geologic features (figs. S1 to S3).

Before performing PCA, we applied a Gaussian filter (2 pixel kernel width) to the individual color bands to mitigate singe-pixel noise. We removed shadows from the maps such that spectral variations within those shadows did not influence the PCA. To remove shadows, we set all pixels with an albedo less than 0.03 to null. Any pixel removed from a single band was removed from all bands. The first principal component (PC1) shows a wide range in albedo, whereas the second (PC2) discriminates changes in the overall spectral slope (from *b′* to *x*), and PC3 indicates variation in the near-ultraviolet (from *b′* to *v*) (figs. S1 to S3). PC4 is the noise floor and reveals the areas where scattered light and incomplete smear correction impact the data at a scale of about 0.5%. The eigenvalues and statistics obtained from the PCA performed on the four MapCam bands is given in table S1.

4. Mapping and classifying geologic features on Bennu

Boulders were mapped with polygons in ARCMAP on Bennu's MapCam color mosaics. The dataset includes 1590 boulders and we consider it a complete, representative population down to 13.55 ± 2.35 m in diameter, although many boulders as small as 1.5 m were also included in this analysis. Separate boulder populations have previously been identified based on albedo, but did not have sufficiently well-constrained photometry to assess their distributions (***Error! Reference source not found.***).

We determined that the histogram of the MapCam *v* band normal reflectance observed for each boulder (Fig. 2A) has a multi-modal distribution by testing whether the data were normally distributed using the Anderson-Darling test, and subsequently using the MCLUST routine in R (***Error! Reference source not found.***) to determine the number of Gaussian components present in the distribution. These tests indicate 99% confidence that the boulder reflectance data presented are not drawn from a population having a single normal distribution. The MCLUST routine identified a 4-component Gaussian mixture as the best fitting model of the data, although any multi-modal distribution is a better fit than a unimodal one. The mean *v* band reflectance and standard deviations of the 4-component model are 0.0412 ± 0.003, 0.0447 ± 0.002, 0.0551 ± 0.004, and 0.075 ± 0.020, and the number of boulders falling into each component are 341, 621, 619, and 10. These values indicate that the dark boulders may comprise two separate populations, or that our thresholding procedures to remove shadows are influencing the spectrophotometric statistics of the lowest-reflectance surfaces.

We distinguished between the low- and high-reflectance boulder populations by thresholding at a *v* band reflectance value of 0.049, which is the median between the two visible peaks of the boulder reflectance distribution. Based on the presence of composition indicators, we classified boulders into Fe-bearing phyllosilicate or pyroxene-bearing boulders on the basis of their *w*-band strength $wbs = w / (0.5v + 0.5x)$, using the median *wbs* value ±3 times the median absolute deviation (MAD) for thresholding. The MAD is a standard statistical method of measuring dispersion and identifying outliers. Fe-bearing phyllosilicate boulders had low *wbs* values (less than $\mathrm{median}(wbs) - 3\mathrm{MAD}(wbs)$), signifying an absorption at 0.7 μm. Pyroxene-bearing boulders had high *wbs* values (greater than $\mathrm{median}(wbs) + 3MAD(wbs)$), signifying an absorption longward of 0.85 μm and a negative b' to *v* reflectance slope. We manually inspected boulders that were close to the classification boundaries to confirm their classification. The four distributions identified by MCLUST have similar mean *v*-band reflectance values to those from the boulder categories identified in this manual classification. The agreement between the different techniques applied improves our confidence that multiple populations of boulder types are present on Bennu.

For the calculations of the b' to *x* spectral slope for boulders and craters, we adapted an equation (***Error! Reference source not found.***) for the MapCam bands:

$$\bar{R}_i = 1 + \gamma(\lambda_i - 0.55\mu m) \qquad \text{eq. S1}$$

where R_i is the reflectance in each band (b', *v*, *w*, *x*) normalized to the *v* band, λ_i is the effective wavelength (in microns) of each band (0.473, 0.550, 0.698, 0.847), and γ is the slope of the fitted line, constrained to a value of unity at 0.55 μm.

We determined the relationship between reflectance and the b' to *x* spectral slope by first conducting an Anderson-Darling normality test for both variables, which indicated ≫99% confidence that neither variable is normally distributed. We therefore conducted a non-parametric correlation test, Kendall's Tau. For Kendall's Tau, as with other correlation metrics, $-1 \leq \tau \leq 1$, and $\tau = 0$ when variables are independent. We found significant evidence ($p \ll 0.01$) to reject the null hypothesis and conclude that dark boulder reflectance and spectral slope have a moderate, monotonically decreasing relationship ($\tau = -0.43$). We conducted the same tests for the bright boulders, among which boulder reflectance and spectral slope have a weaker monotonically decreasing relationship ($p \ll 0.01$, $\tau = -0.29$).

Crater identification within ± 60° latitude was performed using panchromatic PolyCam image data (not MapCam color images) acquired during the Approach and Detailed Survey phases of the OSIRIS-REx mission (***Error! Reference source not found.***,***Error! Reference source not found.***). The Approach images provide global coverage at approximately ~30 cm pixel^{-1} and are suitable for identifying and measuring craters with diameters larger than ~30 m (***Error! Reference source not found.***). The Detailed Survey images provide complete coverage of the surface in latitudes ±60° at low emission angles and with an average of ~5 cm pixel^{-1} (***Error! Reference source not found.***), and permit identification and measurement of craters to diameters <1 m. Images were displayed over Bennu's shape model using the SMALL BODY MAPPING TOOL (SMBT (***Error! Reference source not found.***)), which provides continuously adjustable zoom levels, brightness/contrast control, and manipulation of viewing direction of the shape model. Such manipulation allowed us to set different image parameters to search for features of all scales and brightness levels within the images. Craters were identified by morphology characteristics, primarily via circular depressions, sometimes with particle-size contrasts between the crater interior and exterior. Craters were marked using SMBT's circle or ellipse tool, which records the location and geometry of the circle or ellipse in the coordinate system of the shape model. We subsequently confirmed that >90% of the craters identified in PolyCam images have morphological expression in the OLA data (***Error! Reference source not found.***).

The crater database of sizes and locations was then correlated with the color data set to identify color trends of the craters. Craters were manually registered with Bennu's global color mosaics in ARCMAP. We also debiased the color statistics of overlapping craters, by only using the surface area (pixels) belonging to each crater to calculate statistics. We assume smaller craters were created more recently, thus large craters with overlapping small craters were clipped to remove the shared pixels that belonged to smaller craters. The dataset includes 706 craters; we consider it to be a complete population down to 3.10 ± 0.4 m in diameter, following (***Error! Reference source not found.***). The power law index of the crater size frequency distributions was determined using the methods described in (***Error! Reference source not found.***) for boulder distributions.

5. Analysis of the crater colors, size-frequency distribution, and production function

The absolute spectral slope from the b' to x bands was calculated for the global list of craters. The values for each were then compared directly to the global Bennu average surface b' to x slope (–0.1701 with standard deviation 0.1003). Craters were extracted from the list based on their measured color relative to the global color. The subset of craters that were 1σ redder than average had b' to x slopes greater than –0.0701 (a total of 79 craters met this criterion, and only three were more than 2σ redder). The 255 craters that were 0.5σ redder than average were also extracted.

We determined the relationship between crater reflectance and the b' to x spectral slope by first conducting an Anderson-Darling normality test for both variables, indicating ≫99% confidence that neither variable is normally distributed. Kendall's Tau test indicated significant evidence ($p \ll 0.01$) to reject the null hypothesis and conclude that crater reflectance and spectral slope have a moderate, monotonically decreasing relationship ($\tau = -0.54$).

The differences in the b'/v band ratio of craters categorized by their overall b' to x spectral slope (Fig. 6) were statistically assessed using a one-way analysis of variance (ANOVA). To perform

this test, we assumed that the b' to x spectral slope is dominated by the change from v to x and is thus independent from the b'/v band ratio; the spectral changes in Figure 5 support this assumption. The results, summarized in table S2, demonstrate that the F value, F, is larger than the F statistic, F_{crit}, and so we can reject the null hypothesis. Additionally, the mean and median of each category indicate steeper b'/v band ratios for intermediate b' to x spectral slopes; that is, craters with the most positive and negative b' to x spectral slopes are less blue in the near-UV.

The crater production function is a combination of the expected flux of impactors for a near-Earth object, their typical impact speeds, and the crater scaling expected for impacts into a small rubble-pile asteroid. The flux of impactors in the size range of 1 to 10 m has been measured via bolide detonations in Earth's atmosphere (***Error! Reference source not found.***). The power-law size distributions of these impactors match that for larger bodies (***Error! Reference source not found.***) and are combined to produce an expected flux of impactors per year per square kilometer of a near-Earth asteroid.

We used the gravity-regime crater scaling relationship (***Error! Reference source not found.***,***Error! Reference source not found.***), incorporating the surface gravity of Bennu (0.0000615 m s^{-2} (***Error! Reference source not found.***)) and a typical target grain size of 30 cm. Impactor density was assumed to be 2300 kg m^{-3}, target bulk density was assumed to be that measured for Bennu of 1190 kg m^{-3} (***Error! Reference source not found.***), target grain density was assumed to be 2300 kg m^{-3}, solid target disruption energy was assumed to be 1000 J/kg, and an impact speed of 18.5 km s^{-1} was used to represent the mean impact speeds between near-Earth asteroids (***Error! Reference source not found.***).

6. Calculating spectral slopes across individual dark boulders

We examined nadir MapCam images taken during the re-fly of Baseball Diamond Flyby 2 (26 September 2019) and identified 220 large boulders between ±20° in latitude (boulders outside of this latitude range were imaged with emission angles >20°). The rim of each boulder was manually traced in MapCam images. Based on the manually traced boulder outline, we calculated the azimuthal angle that maximizes the blue-to-red color variation within each boulder. We calculated the difference in the average b' to x spectral slope between the two regions within the outline of each boulder, which is divided by a line segment with a variable angle crossing the centroid of a boulder. Pixels with incidence/emission angles > 60° and I/F < 0.01 were discarded from the calculation. The optimal angle was identified via a grid-search between 0° to 360° range with 30° intervals in each boulder image. The determined angles were converted to azimuthal angles shown in fig. S11 by georeferencing the images to an equirectangular projection.

Fig. S12 shows intra-boulder variation. Whether such color variation could be a product of the illumination conditions (e.g., inclusion of sub-pixel scale shadows) was evaluated by calculating the root mean square (RMS) error of the radiance factor using multiple images taken with slightly different viewing angles during the flyby sequence. The distribution of the RMS deviation showed limited correlation with the observed intra-boulder color variation; thus, the observed variation should at least partly reflect the surface property of boulders.

7. Spectrophotometric trends and comparison between Bennu and Ryugu

The *I/F* distribution (fig. S13) was calculated by using the global observation images: PolyCam images of Bennu taking during the OSIRIS-REx mission's Approach and Preliminary Survey phase (20181113T041412S224_pol_iofL2pan to 20181113T083212S153_pol_iofL2pan) and ONC-T (Optical Navigation Camera) *v* band images of Ryugu taken during the Hayabusa2 mission's Box-A Operation (hyb2_onc_20180712_064513_tvf_l2d to hyb2_onc_20180712_134452_tvf_l2d). These images were chosen due to their similarity in resolution (~2 m pixel^{-1}) and phase angle (18–19°), minimizing observational biases between the OCAMS and ONC data sets. To account for the different shapes of the two asteroids, the *I/F* values were photometrically corrected to an observation geometric condition (*i, e,* α) = (18°, 0°, 18°). Similar-resolution shape models (~3 m facets) were used for the correction (stereophotoclinometry v20 (***Error! Reference source not found.***) for Bennu and stereophotoclinometry v20180717 for Ryugu). The photometric functions and parameters were taken from the fitting conducted by using images taken under a wide range of conditions (***Error! Reference source not found.***, ***Error! Reference source not found.***). Pixels with incidence or emission angles >60° and *I/F* < 0.01 were discarded because of the uncertainties in the photometric correction and their low signal-to-noise.

I/F pixels were mapped to an equirectangular projection. Each mesh in the equirectangular projection was weighted with a cosine of latitudes to account for the areal distortion to create the areal frequency histogram. Each histogram was normalized by its total area. The photometrically corrected images were binned in 32 × 32 pixel bins to calculate the distribution at a pixel scale of ~64 m.

The same method was applied to the color distributions (fig. S13). We used color images from MapCam during the OSIRIS-REx Baseball Diamond Flyby 2b for Bennu and ONC-T the Box-A Operation for Ryugu (***Error! Reference source not found.***). The difference in the resolution was compensated for by conducting an 8 × 8 pixel binning of the MapCam images.

For the comparison between Bennu and Ryugu, the b' to *x* spectral slope was calculated as:

$$\frac{b'/v - x/v}{\lambda_{b'} - \lambda_x} \qquad \text{eq. S2}$$

The effective wavelengths are slightly different with the MapCam and ONC-T filters ($\lambda_b = 0.4798$ μm, $\lambda_v = 0.5489$ μm, and $\lambda_x = 0.8573$ μm for ONC-T (***Error! Reference source not found.***)). This effect was quantified by calculating the difference in band ratios of the 398 C-complex asteroids surveyed by Small Main-Belt Asteroid Spectroscopic Survey, Phase II (SMASS2) (***Error! Reference source not found.***) using the respective wavelengths of the two cameras. The difference in the band ratios was confirmed to be ~1% (RMS error of 1.1 % for b'/v and 0.99% for x/v) and thus would not affect our qualitative results.

A Student's t-test was used to assess the significance of the difference between the means of Gaussian-like equatorial and mid-latitude color distributions on Bennu (fig. S13D). The means for Ryugu and Bennu are significantly different with $p \ll 0.01$. This trend holds after the photometric correction (***Error! Reference source not found.***) ($p \ll 0.01$). Thus, the slight bluing of Bennu's equator relative to the mid-latitude regions is likely not due to observational biases.

8. Spectral Analogs of Bennu

Although carbonaceous meteorites are expected to be a reasonable compositional analog for Bennu, the reflectance of Bennu is lower than that of most meteorite samples. To reproduce the spectral reflectance properties and variations seen on Bennu, we produced a series of physical and simulated analogs consisting of two-component mixtures of an Mg-rich phyllosilicate, saponite, magnetite and one of two forms of carbon, graphite or lampblack (shown in fig. S4 C and D).

Simulated analogs (fig. S4 D) used the samples and procedures outlined in (***Error! Reference source not found.***). For physical analogs, we produced a series of them spanning a range of carbonaceous material abundances (0–10 wt.%). We used saponite (containing ~25 wt.% dolomite) as the primary phyllosilicate because Bennu may have been extensively aqueously altered, and as aqueous alteration proceeds, the abundance of saponite to serpentine in carbonaceous chondrites increases, and the phyllosilicates become increasingly Mg-rich (e.g., ***Error! Reference source not found., Error! Reference source not found., Error! Reference source not found., Error! Reference source not found.***). Because it is not possible to extract enough carbonaceous material from carbonaceous chondrites to produce sufficient quantities of simulants, we used fine-grained amorphous carbon or graphite because it is not possible to extract enough carbonaceous material from chondrites to produce sufficient quantities of simulants. The amorphous carbon (lamblack) and graphite are spectrally featureless in the 0.3–5 μm region (***Error! Reference source not found.***), and both induce a bluing (reflectance decreasing toward longer wavelengths) in mixtures with phyllosilicates (***Error! Reference source not found., Error! Reference source not found.***), (fig. S4 C).

The series of saponite+lampblack and saponite+graphite mixtures that we produced have carbonaceous phase abundances that encompass (and exceed) the range of carbonaceous phase abundances in carbonaceous chondrites of types CI1 and CM1-2 (***Error! Reference source not found.***).

Samples used: Our mixtures included a natural (but partially processed by the supplier) saponite (our sample #SAP105), a fine-grained synthetic lampblack (our sample #LCA101), and a synthetic graphite (our sample #GRP102). Sample sources were:

- SAP105 is sourced from Amargosa Valley, CA-NV, USA. It was provided as a fine-grained beige powder by IMV Minerals (Lhoist North America) and is marketed under the trade name Imvite.
- LCA101: Johnson Matthey, #14237A, <0.021 μm particle size. GRP102: Johnson Matthey, #10130A, –300 mesh, 99.5% pure.

Preparation of mixtures: To produce samples with intimately mixed phyllosilicates and opaques, we adapted a procedure developed (***Error! Reference source not found.***) for Bennu analogs.

The as-received endmembers were all fine-grained (<45 μm), so no additional sample preparation was required. Mixtures were prepared by weighing out endmembers using a balance with an accuracy of ±0.1 mg. Approximately 50 grams of each mixture were produced. Each mixture was placed into an alumina mortar and pestle and ground together for one minute to remove clumping. The powders were then mixed with reverse osmosis (RO) water at a volumetric ratio of roughly

2:1 water:powder in a stainless steel cup with agitators. The resulting slurries were further blended with a commercial-grade drink mixer for roughly 10 minutes and then poured into aluminum trays with crenulated bottoms. The mixtures were then heated to 150°C in air and kept at that temperature for 4 days using a drying oven. The slurries were initially ~10 cm thick, and the heating process resulted in a very large volume loss and formation of mostly few-centimeter chunks due to desiccation cracking about 1 cm deep. The resulting chunks had a smooth cuspate surface with a surface coating of light-colored precipitate (likely halite), and a few vesicles (up to ~3 mm in diameter). The upper surfaces of the chunks were scraped with a razor blade to remove the salt crust. A portion of the sample was retained as-is, with the upper surfaces additionally sanded with 60 grit aluminum oxide sandpaper to produce a matte surface. Other portions of the sample were ground by hand in the alumina mortar and pestle and dry-sieved to produce <1000 and <45 µm powders, also after removing the salt crusts. This resulted in four different types of samples for spectral analysis: flat-matte surfaces, crenulated surfaces, <1000 µm powders, and <45 µm powders.

Scanning electron and optical microscopy indicated that the lampblack was not fully dispersed in the mixtures. The samples showed some areas of clumped lampblack with the larger aggregates about 30–50 µm in diameter. Carbon and carbonaceous material mapping of CM chondrites shows that carbon-rich domains range in size from <1 µm to a few to tens of microns and are heterogeneously distributed (e.g., ***Error! Reference source not found.***, ***Error! Reference source not found.***), so that incomplete disaggregation of the lampblack more closely reproduces carbonaceous chondrite matrix textures than complete disaggregation would.

Supplementary Figures

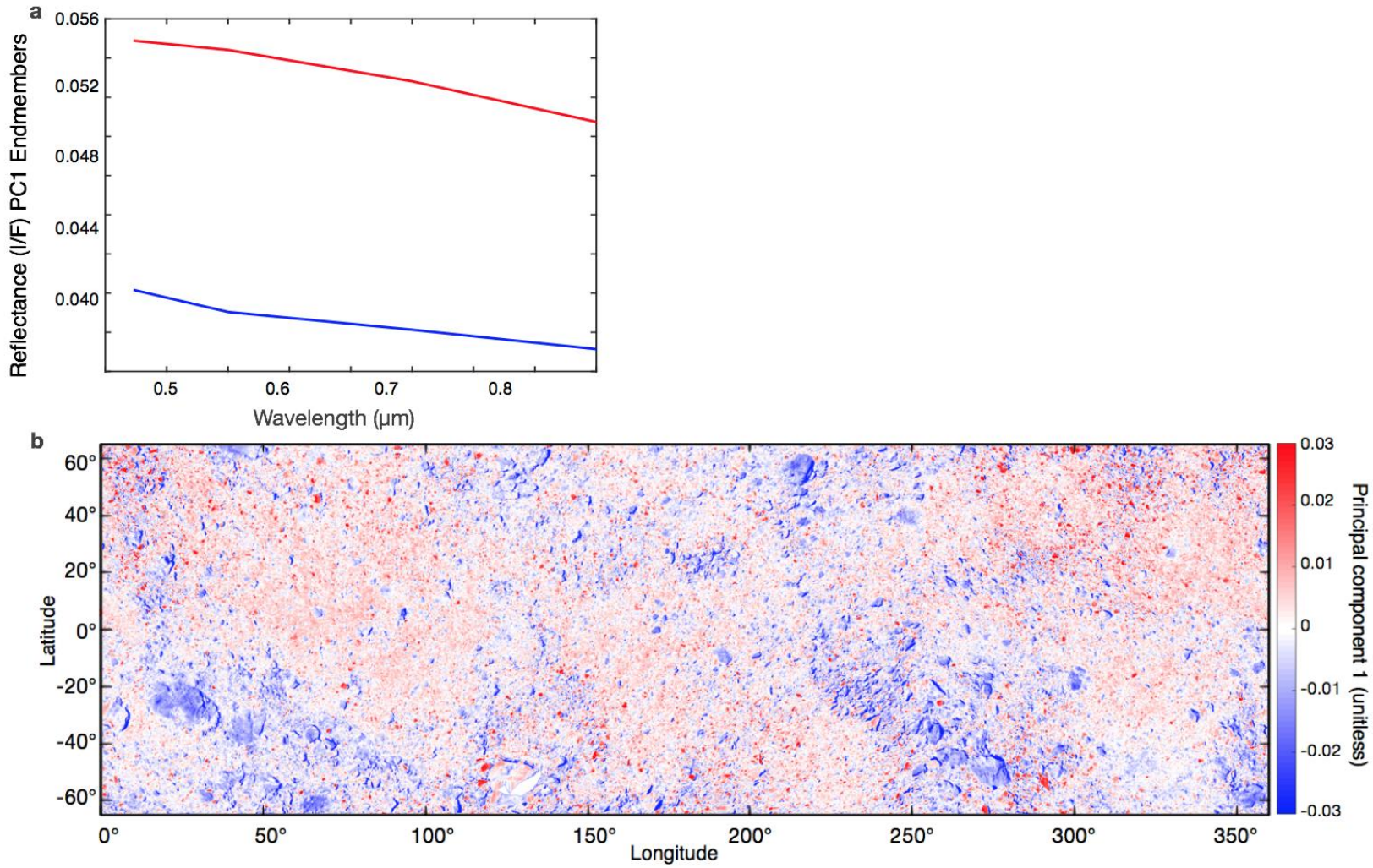

Fig. S1. Principal Component 1. (**A**) The average spectra for the high and low endmembers of the histogram of PC1. (**B**) PC1 mapped across the surface of Bennu. The red and blue spectra correspond with high and low values in the map of PC1, respectively. The overall change in albedos across Bennu is captured by PC1, which tracks with the *v* band normal reflectance.

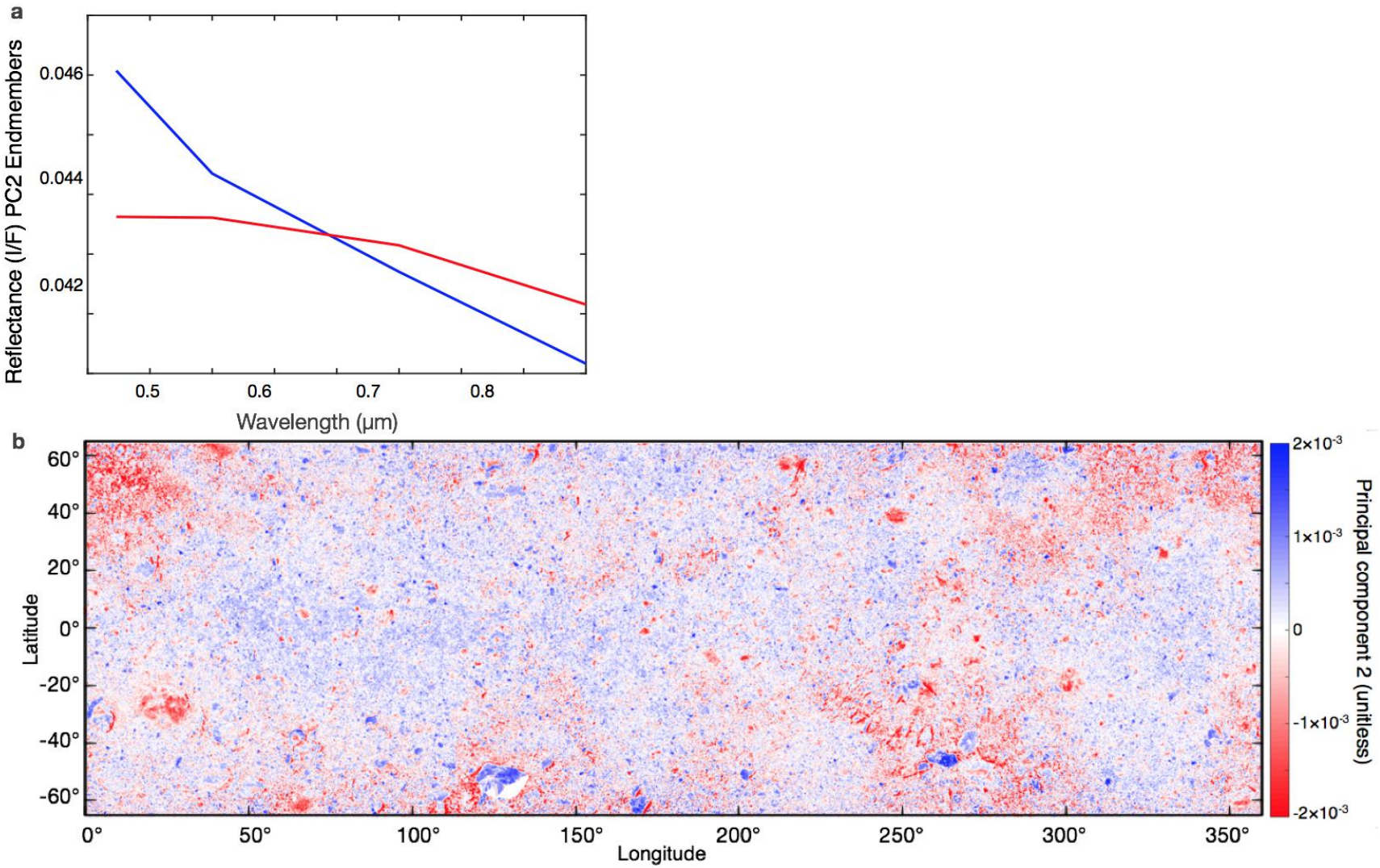

Fig. S2. Principal Component 2. (**A** and **B**) Same as in fig. S1, but for PC2. The overall spectral slope (from b' to x) appears to drive the variance of PC2 and tracks the b'/x band ratio.

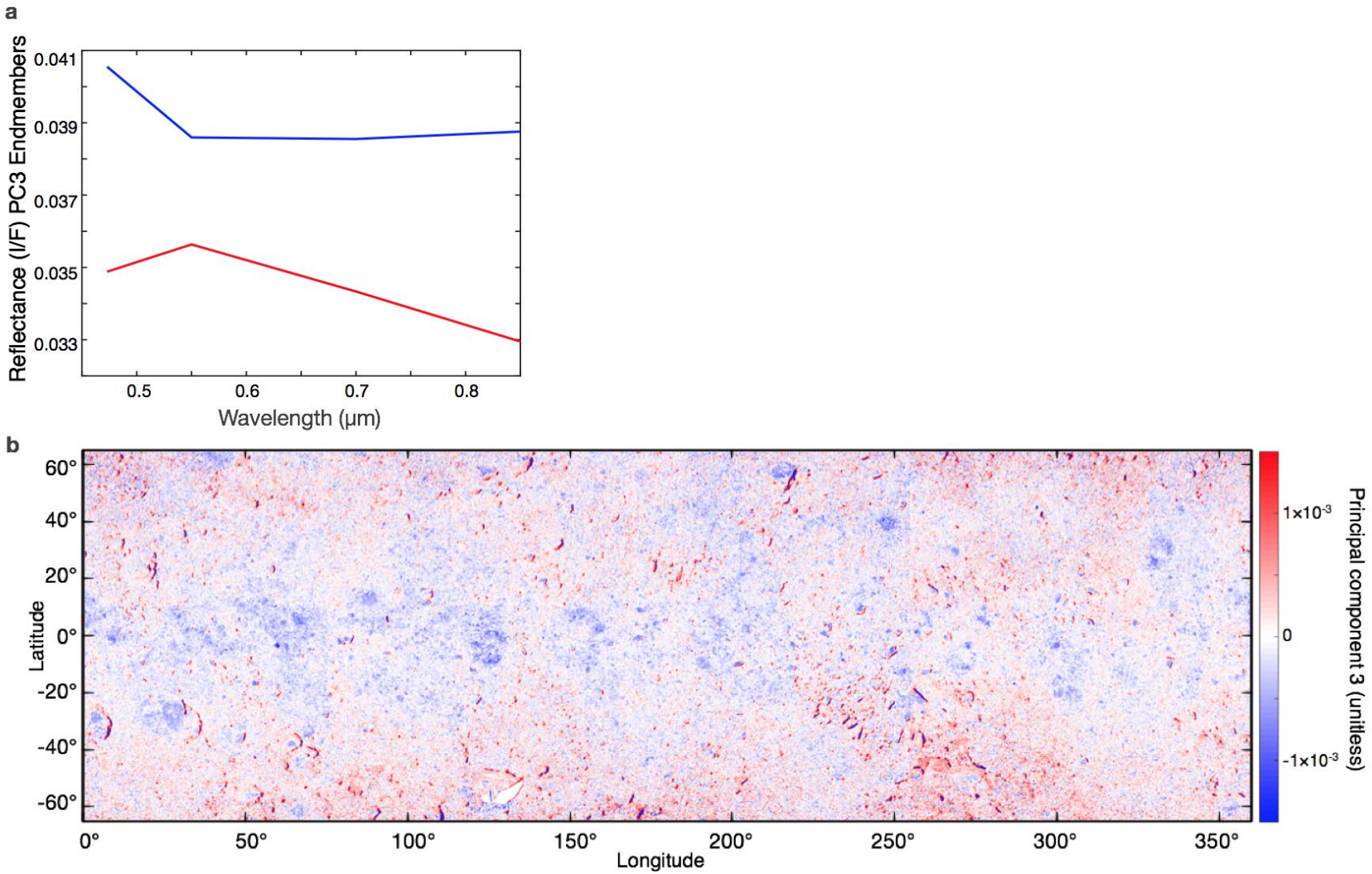

Fig. S3. Principal Component 3. (**A** and **B**) Same as in fig. S1, but for PC3. Most spectral variance in PC3 corresponds to an upturn or downturn in the *b′* band and tracks the *b′/v* band ratio.

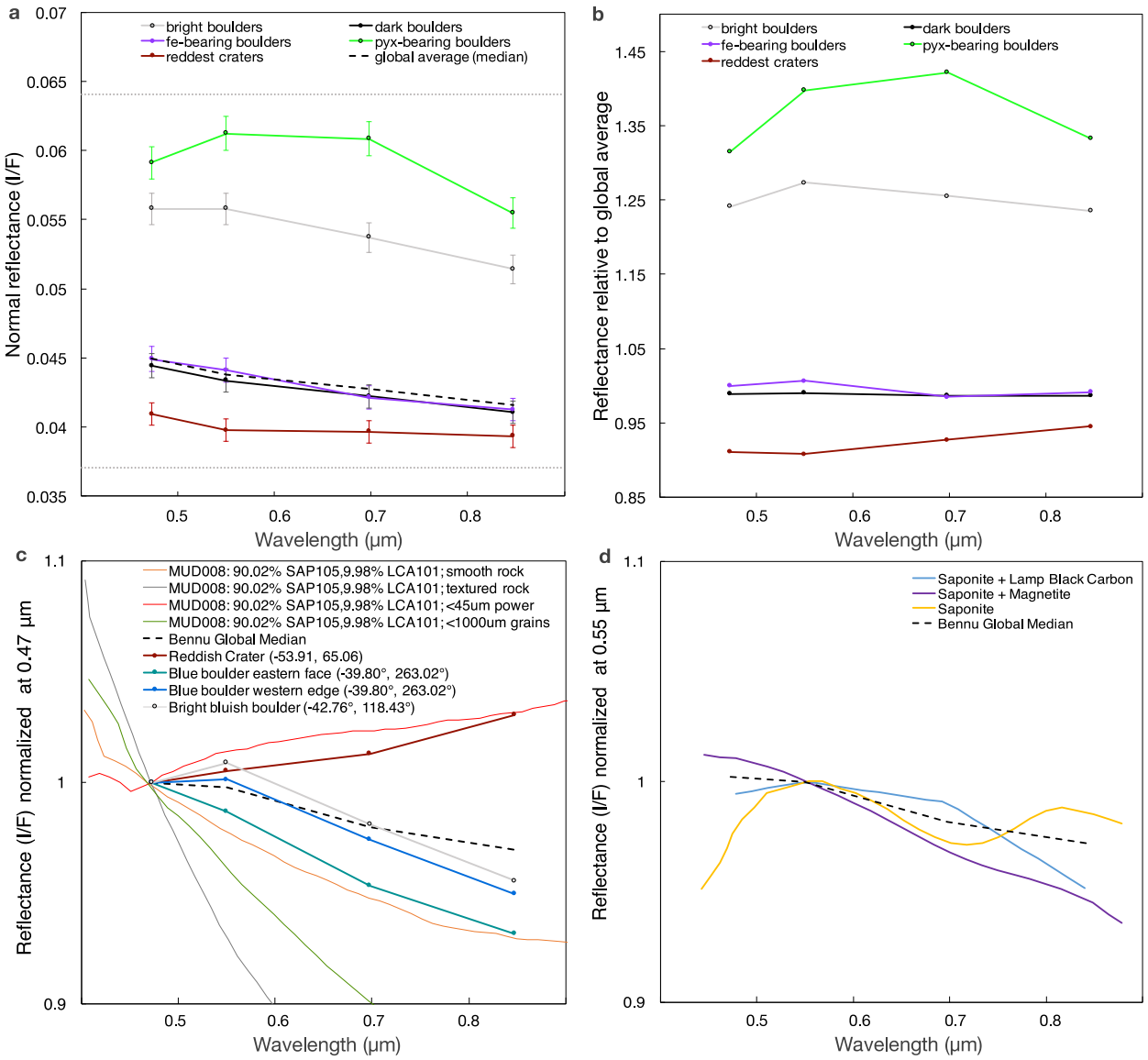

Fig. S4. Reflectance of boulders, craters, and Bennu analogs. (**A**) Average (median) spectra in absolute normal reflectance of each color unit identified in Table 1. Error bars represent that 2% relative radiometric uncertainty in MapCam data and the light gray dotted lines encompass the 5% range of absolute radiometric uncertainty. (**B**) Same spectra shown in (A) ratioed with the global median spectrum of Bennu, which removes the relative and absolute uncertainties. (**C**) MapCam photometric spectra (solid circles connected by solid lines) for various color units as compared with Bennu's global spectrum (black dashed line) and laboratory samples (solid lines; labeled MUD008) of the phyllosilicate saponite (~90%) mixed with lampblack carbon (10%) and prepared in different textures. (**D**) The serpentine saponite combined, modeled in intimate mixtures with both magnetite and simulated fine-grained lampblack carbon. The models demonstrate the bluing effects of both magnetite and carbon (in this case, lampblack); the bluing effects are expected to vary depending on grain size, abundance, and "host" serpentine. Bennu's global spectrum (black dashed line) has a blue spectral slope that falls between both mixtures.

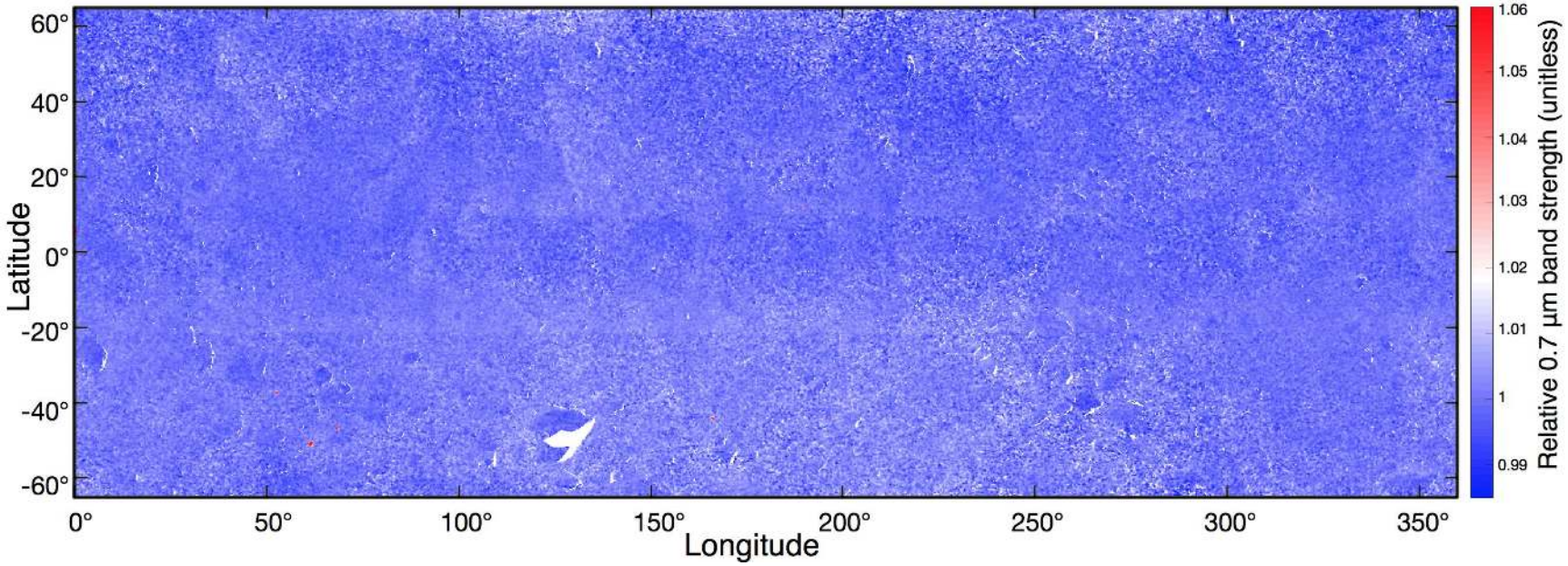

Fig. S5. MapCam mosaic (25 cm pixel^{-1}) of the relative band strength at 0.7 µm. Some larger dark boulders appear to have a weak (~1%) absorption feature (values <1). Although this weak absorption feature is at the radiometric precision of the MapCam instrument, its spatial coherence with individual boulders provides confidence that it is real. However, at the 1% level, minor artifacts, such as stray light (which causes linear artifacts at image seams), are also visible. Pyroxene-bearing boulders have band strengths at 0.7 µm >1 and appear as meter-scale red patches.

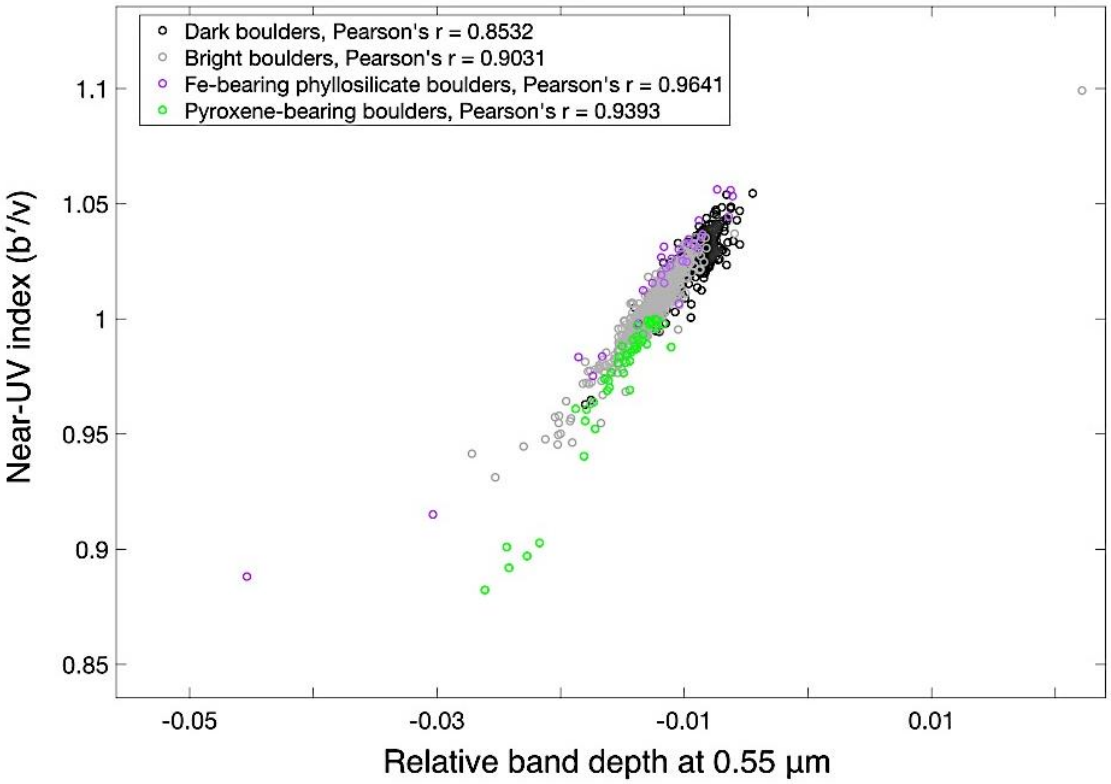

Fig. S6. The *b′/v* band ratio (near-UV index) as a function of the relative band depth at 0.55 µm for the different boulder types identified on Bennu. These quantities are linearly correlated for the different boulder types. The upturn in the near-UV observed in the spectra of some boulders may be the result of an absorption feature at 0.55 µm.

Fig. S7. PolyCam image (~5 cm pixel^{-1}) of the primary OSIRIS-REx sample site, Nightingale (white circle), acquired on 12 April 2019. This location appears smoother and is less well resolved than the bulk of the asteroid's surface. The texture of Nightingale is representative of many of the small reddish craters on Bennu. The image was taken from a distance of 2.8 km. The field of view is 39.6 m on each side.

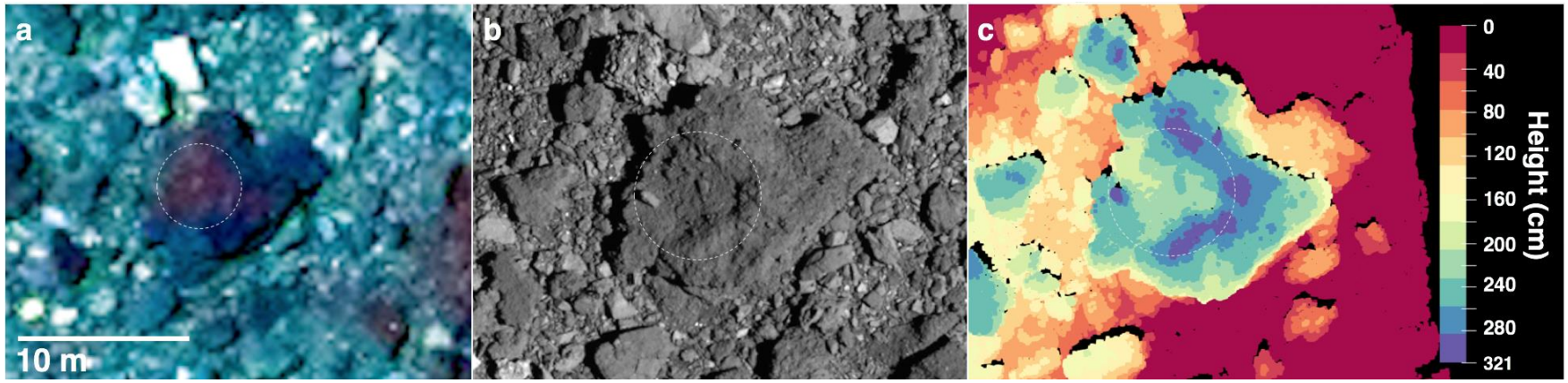

Fig. S8. Example of a crater on a boulder. (**A**) MapCam RGB false-color composite (same stretch as Fig. 3A) of a boulder with a putative crater (white dashed line), (**B**) as visible in a higher-resolution PolyCam image (5.25 cm pixel^{-1}), and (**C**) the local OLA DTM. The recessed crater in this boulder is spectrally redder than its surroundings.

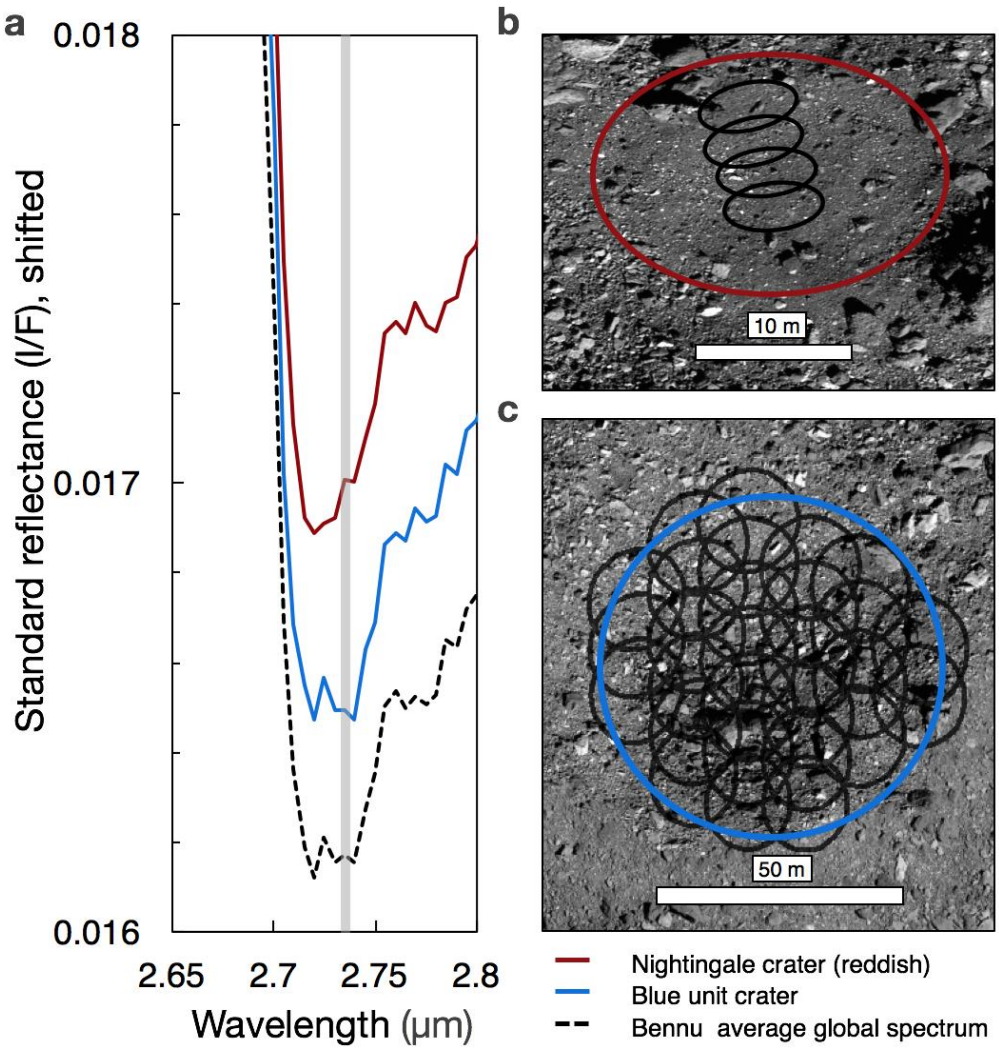

Fig. S9. (**A**) Non-normalized OVIRS spectra for Nightingale crater (solid red line), the blue unit crater at 1.06°lat, 152.75°lon (solid blue line), and Bennu's global average (dashed black line), corrected to standard reflectance conditions (30°, 0, 30°). The red and blue spectra are vertically shifted for display by –0.001 and –0.0033, respectively. The wavelength range was chosen to emphasize the minima of the 2.7-μm band associated with hydrated phyllosilicates. The gray vertical line indicates the minimum band position for the Bennu's global average, at 2.735 μm. For Nightingale crater, the band minimum is sharper, and its position is shifted (~15 nm) toward shorter wavelengths, compared to the global average. The blue unit crater's average spectrum has the same hydration band minimum as the global average at 2.735 μm. Still, the shape of the feature is sharper than that of the global average. The global average spectrum was obtained from all Detailed Survey OVIRS spectra (footprint size, 20 m) from the 12:30 PM local solar time Equatorial Station (09 May 2019). (**B**) Footprints of the four spectra of Nightingale averaged together for the red spectrum in (A). Data are from the Recon A phase of the mission (12 Oct. 2019), where the OVIRS footprints span ~6 m. (**C**) The footprints of the 28 individual spectra from 12:30 PM local solar time Equatorial Station were used to determine the blue spectrum in (A), which is bluer than the global average by a factor of ~3 in the range 0.55–2 μm (when normalized at 0.55 μm).

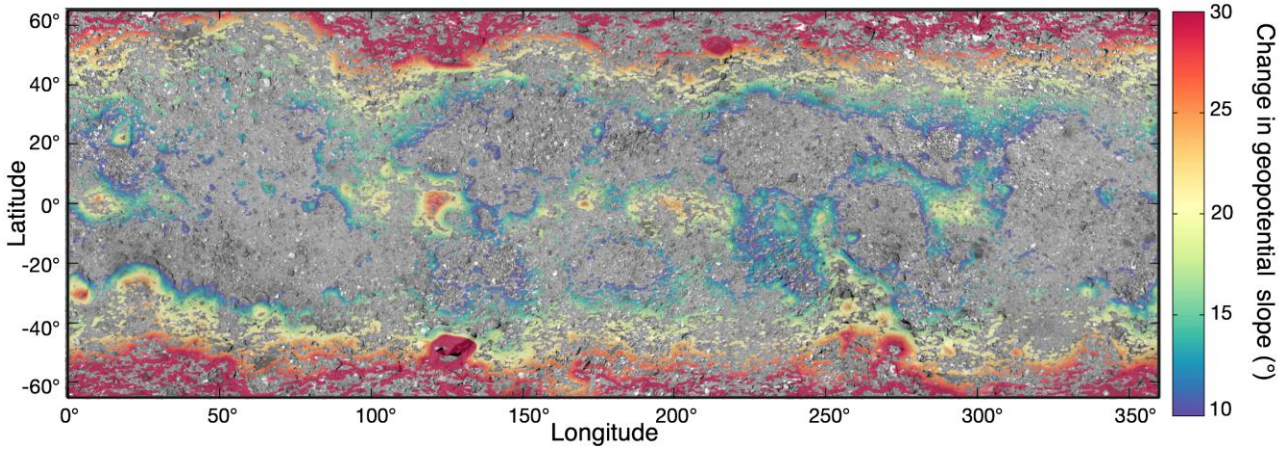

Fig. S10. The change in geopotential slope across the surface of Bennu as the spin period decreases from 5 hours to the present-day 4.3 hours over the past 200,000 years (***Error! Reference source not found.***). The isolated region near 0°lat, 120–150°lon coincides with the presence of the equatorial blue crater units.

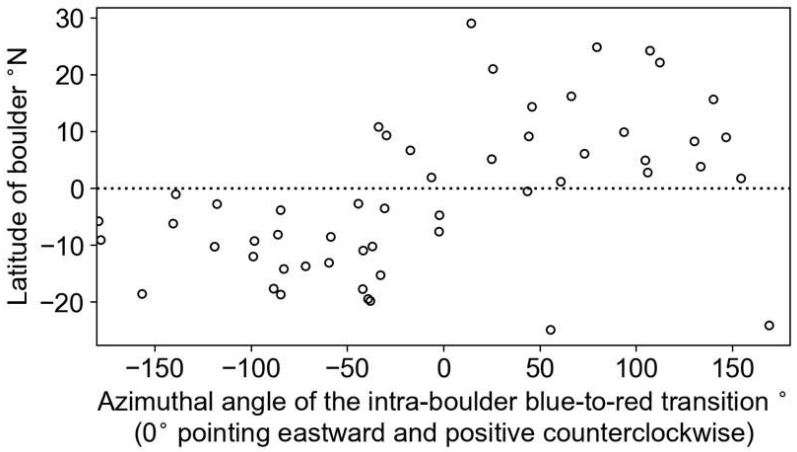

Fig. S11. Azimuthal angles of the intra-boulder color variation plotted against situated latitudes of boulders.

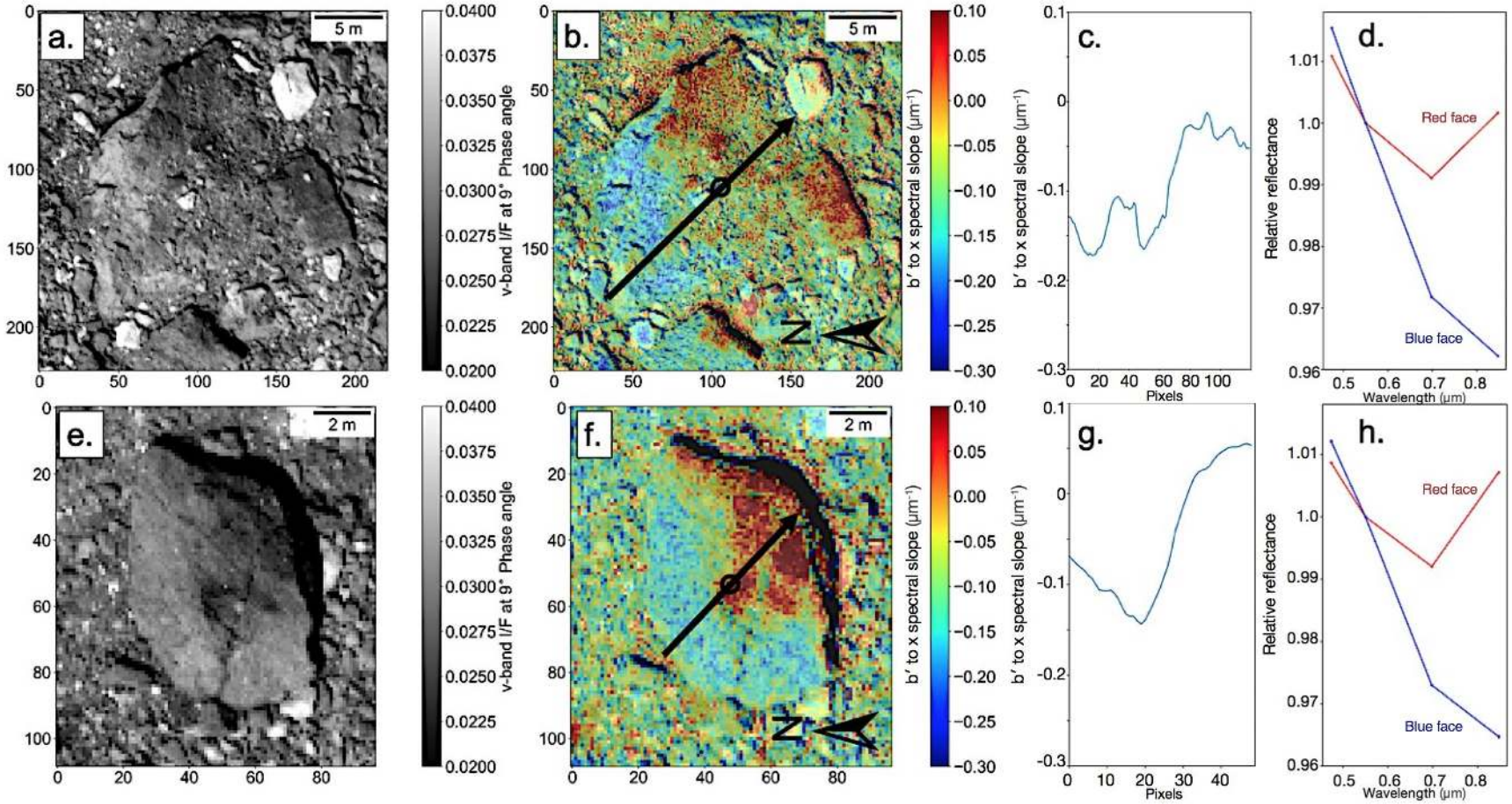

Fig. S12. Intra-boulder color distribution of boulders. (**A**) Image of a boulder situated at 20°S, 255°E (20190926T173725S586_map_iofL2v_V005.bvwx). (**B**) The *b′* to *x* spectral slope within the boulder. The arrow shows the calculated direction that maximizes the blue-to-red color variation. The circle indicates the centroid of the boulder. (**C**) The profile of the *b′* to *x* slope along the arrow shown in (B). The profile is smoothed by averaging over 20 pixels. (**D**) The *v* band normalized spectra of bluer and redder faces of the boulder. (**E** to **H**) Same as (A) to (D) for a boulder situated at 10°S, 260°E. Bluer surfaces tends to be brighter. The spectral difference between blue and red faces shows that the intra-boulder color variation is characterized by the heterogeneity in VIS spectral slope and the possible weakening of the 0.7-μm absorption, whereas the degree of UV upturn is relatively uniform.

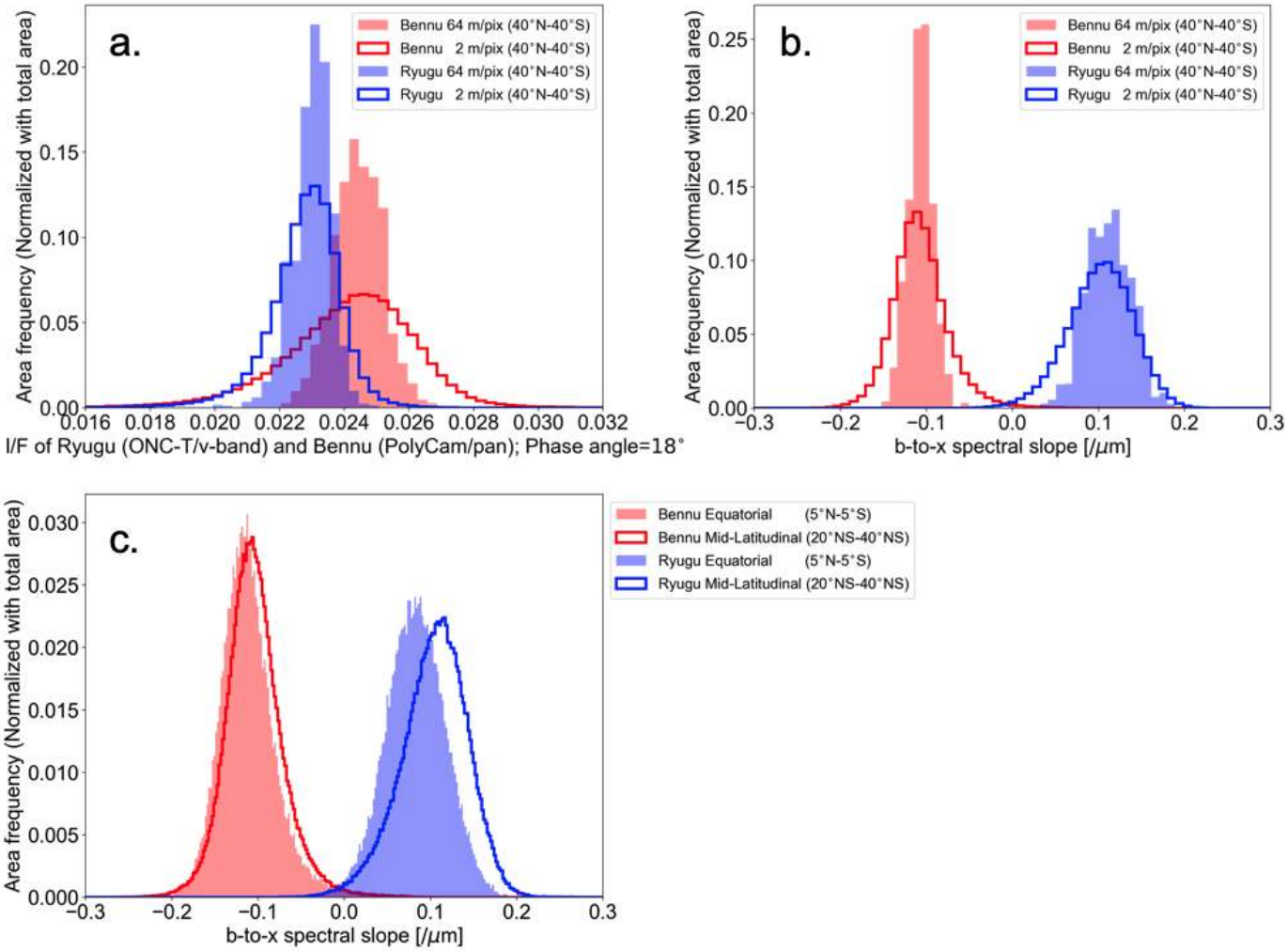

Fig S13. Comparison of the reflectance and color distribution between Bennu (red) and Ryugu (blue). The areal distribution of (**A**) reflectance and (**B**) spectral slope observed at ~2 × 2 m^2 and ~64 × 64 m^2 resolution. Owing to the slightly different effective wavelengths of the blue filters of OCAMS and ONC-T, spectral slopes are determined from *b* to *x* for Ryugu and *b′* to *x* for Bennu. (**C**) The change in the spectral slope distribution when averaged zonally at different latitudes.

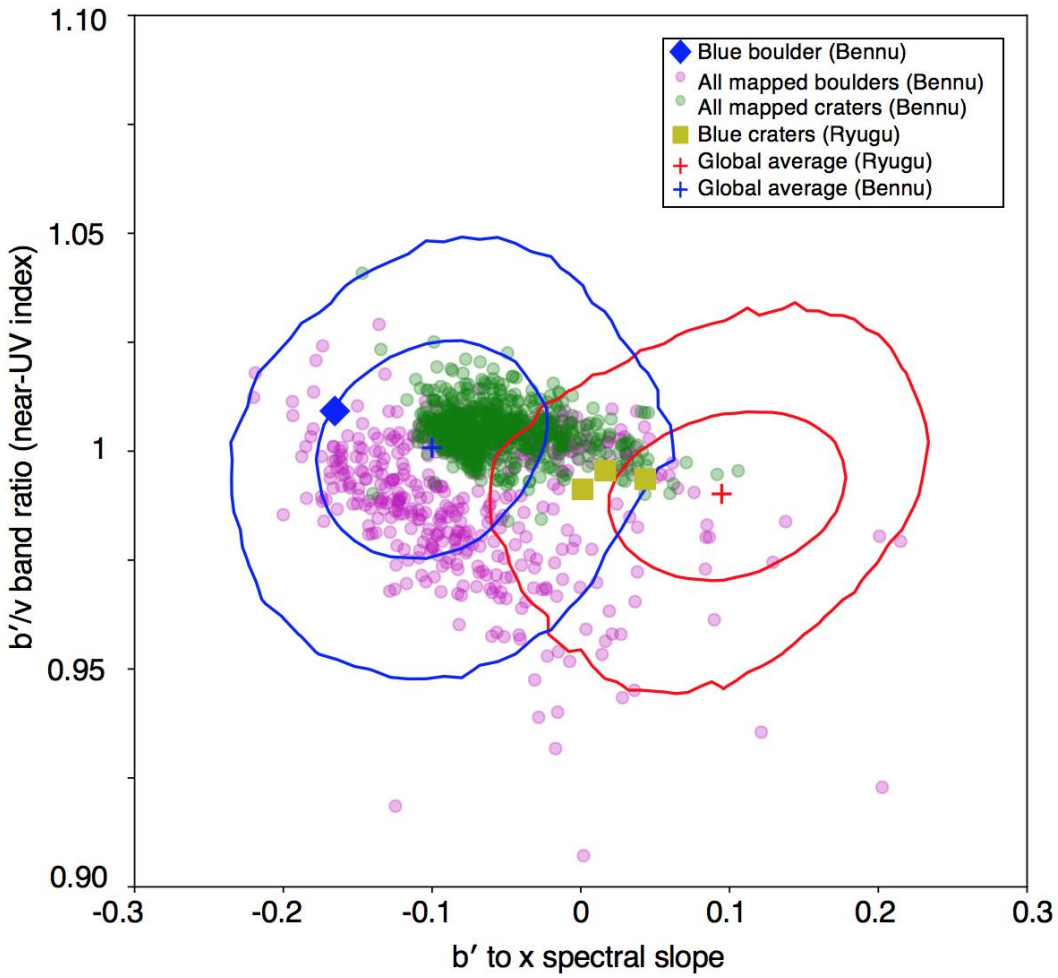

Fig S14. Comparison of Bennu's colors with the color of craters on Ryugu. The color of blue craters on Ryugu from (*70*) (yellow squares) compared to craters (green circles) and boulders (magenta circles) on Bennu. The *x* axis is the *b′* to *x* spectral slope, and the *y* axis is the *b′/v* band ratio (near-UV index). Bennu and Ryugu's average global values (crosses) are shown for context, with ellipses that indicate the variation for 68% and 95% coverage.

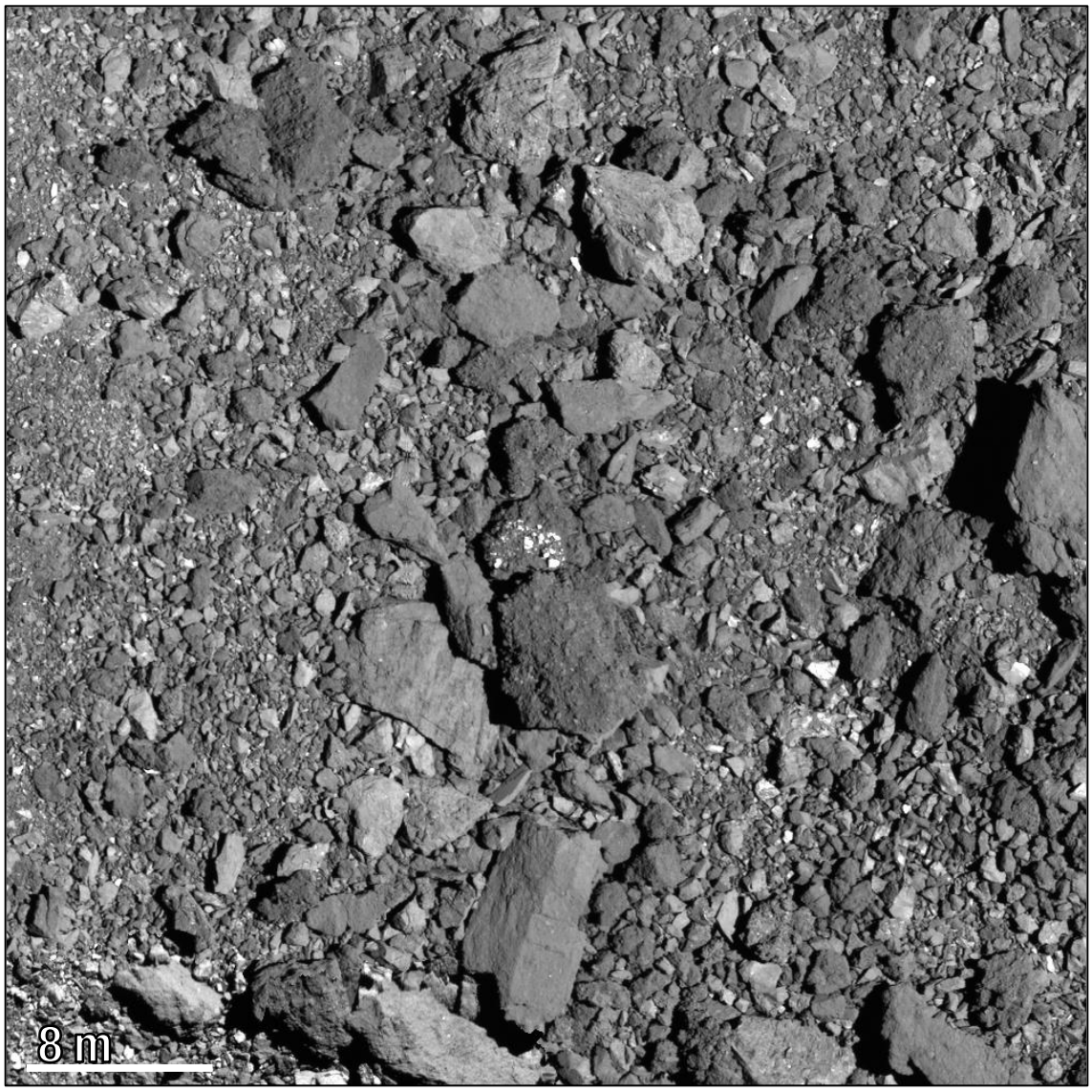

Fig S15. Regional context for the boulder shown in Fig. 3I. A 50 m × 50 m subset of the global mosaic of Bennu (***Error! Reference source not found.***), centered on the boulder shown in Fig. 3I (bright clasts in a dark matrix). Although there are small bright boulders in this region, there are none in the immediate vicinity of this boulder, nor are there any on the neighboring boulders. This provides confidence that the bright clasts in the boulder shown in Fig. 3I are embedded in, rather than perched upon, the boulder.

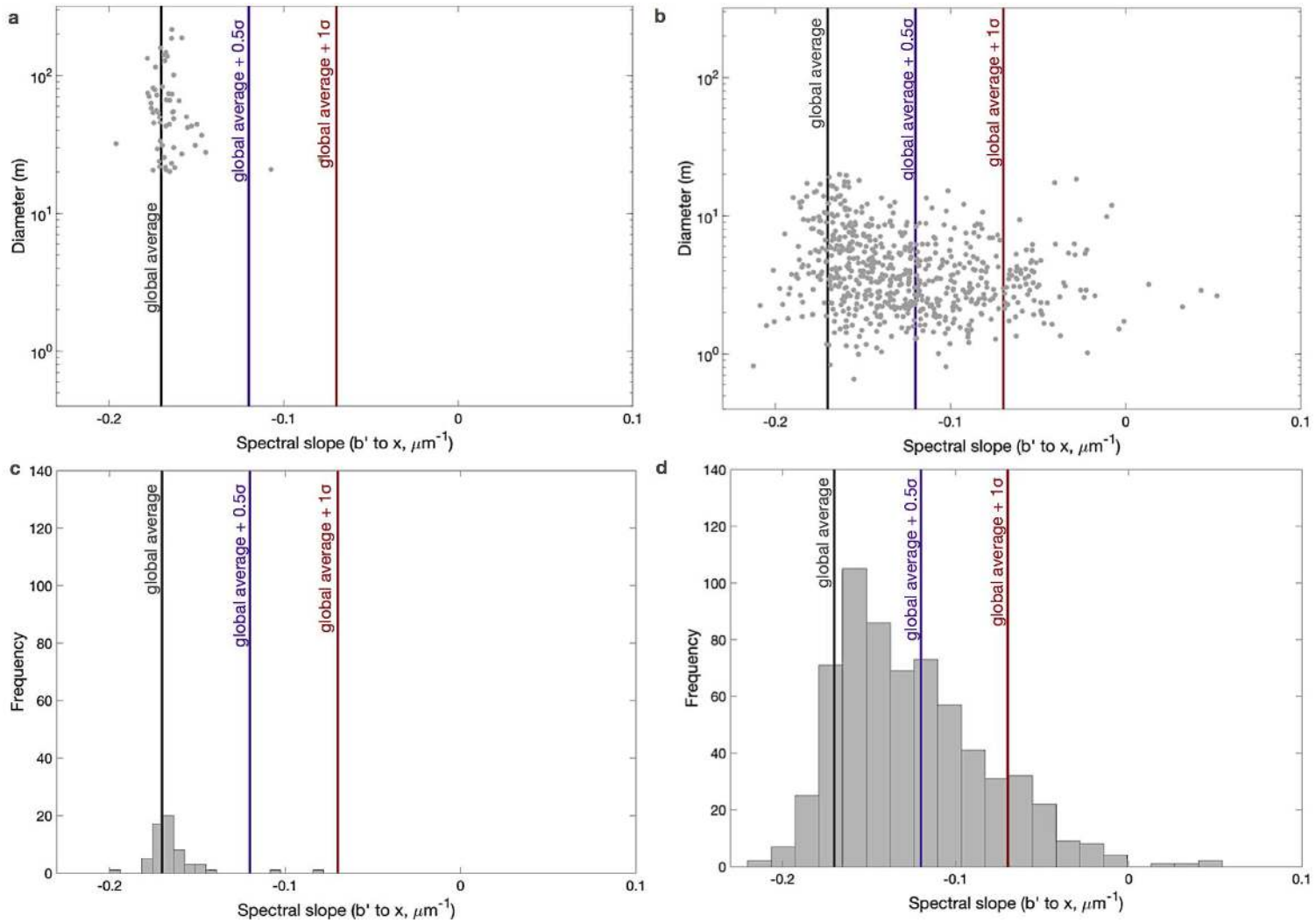

Fig S16. Supporting information for the relationship between spectral slope and crater size and frequency. (**A**) Crater diameter plotted against median b' to x spectral slope, for craters >20 m. (**B**) Crater diameter plotted against median b' to x spectral slope, for craters ≤ 20 m. (**C**) The b' to x spectral slope distribution of craters on Bennu, for craters >20 m. (**D**) The b' to x spectral slope distribution of craters on Bennu, for craters ≤20 m. When we separate out the largest craters on Bennu (>20 m), the trends between spectral slope and crater size and frequency, as highlighted in Fig. 5, still hold.

Table S1. Summary statistics obtained from the PCA performed on the four MapCam bands, including the percentage of the total variance in each PC as well as the eigenvalues, per band, for each PC.

	PC1	**PC2**	**PC3**	**PC4**
b′ eigenvalues	0.514	0.76	–0.378	0.124
v eigenvalues	0.52	0.077	0.708	–0.471
w eigenvalues	0.5	–0.373	0.18	0.76
x eigenvalues	–0.463	–0.527	–0.569	–0.429
% PC variance:	99.3	0.43	0.17	0.089

Table S2. Summary of ANOVA for different crater *b′/v* band ratios, categorized by their overall *b′* to *x* spectral slope (Fig. 6). μ is the global average *b′* to *x* spectral slope of Bennu, and σ indicates the standard deviation.

a. Summary of statistics

Category	*Count*	*Sum*	*Mean*	*Median*	*Variance*
***b′/v* band ratios for:**					
μ > craters *b′* to *x* slope	91	91.2227	1.0024	1.0028	3.57×10^{-5}
μ + 0.5σ > craters *b′-x* slope ≥ μ	366	367.3244	1.0036	1.0037	4.65×10^{-5}
μ + 1σ > craters *b′* to *x* slope ≥ μ + 0.5σ	174	175.0637	1.0061	1.0054	6.21×10^{-5}
craters *b′* to *x* slope ≥ μ + 1σ	75	75.2571	1.0034	1.0025	8.32×10^{-5}

b. ANOVA

Variation source	*Sum of squares*	*Degrees of freedom*	*Mean square*	*F*	*p-value*	F_{crit}
Between Groups	0.0011	4	0.0003	5.0612	0.0005	2.3846
Within Groups	0.0371	701	5.29×10^{-5}			
Total	0.038	705				

Caption for data S1. Comma separated value (CSV) list of the boulders used in this study. The first row are column headings and subsequent rows are boulder data. A description each column heading, in single quotes, is given parenthetically here: 'sequential_id' (arbitrary unique id), 'area_m^2' (area of the polygon used to trace boulder in units of m^2); 'center_latitude' (polygon central latitude in units of degrees, domain ±90º); 'center_longitude' (polygon central longitude in units of degrees, domain 0–360º); and 'classification' (determined by the boulder classification scheme described in this study).

Caption for data S2. CSV list of the craters used in this study. The first row are column headings and subsequent rows are crater data. A description each column heading, listed in single quotes, is given parenthetically here: 'sequential_id' (arbitrary unique id), 'radius_km' (radius of the circle used to trace the crater, in units of km); 'center_latitude' (circle central latitude in units of degrees, domain ±90º); 'center_longitude' (circle central longitude in units of degrees, domain 0–360º).

Caption for data S3. Text file list of all the OCAMS MapCam long exposure images used to produce the maps in Fig. 1.